공학석사 학위논문

Facile synthesis of Ni–Cu phosphorous as an efficient water oxidation electrocatalyst via electrodeposition

전기도금을 통한 간편한 니켈-구리 인화촉매의 제조와 물 산화반응에의 응용

2017년 2월

서울대학교 대학원

화학생물공학부

김 병 근

Abstract

Facile synthesis of Ni-Cu phosphorous as an efficient water oxidation electrocatalyst via electrodeposition

Byung Keun Kim

Department of Chemical and Biological Engineering

College of Engineering

Seoul National University

Electrochemical water splitting has attracted great attention since it is the most promising strategy for large-scale hydrogen production. Efficient electrolysis is limited due to sluggish kinetics of oxygen evolution reaction (OER), however, as well as high cost of state-of-art precious metals. Hence, numerous researchers endeavored to develop highly active electrocatalyst with low cost. Indebted to this, this study was focused on synthesis of nickel-copper phosphorous electrocatalyst with high OER activity via facile electrodeposition. Optimization of preparation condition confirmed that nickel-copper phosphorous prepared with electrolyte containing 199:1 of Ni^{2+}/Cu^{2+} ratio exhibited best performance, which even surpasses the OER activity that of NiP, which is already reported as efficient OER

catalyst. Suitable Cu addition resulted in lowered Tafel slope and charge transfer resistance compared to NiP. XPS study revealed that Cu addition enhances the role of Ni-P supporting layer, which lies right underneath the OER active, but thermodynamically unstable Ni hydroxide species. Ni spectra showed higher high-valence-state Ni species when Cu was added in the catalyst. The catalyst was electrodeposited with nano-crystalline phase, explained by XRD patterns. According to SEM image, nickel-copper phosphorous has film-like morphology, with uniform element distribution throughout the surface. The catalyst showed excellent robustness up to 18 hrs of OER operation, as well as high Faradaic efficiency over 99%.

Keywords: nickel-copper phosphorous, oxygen evolution reaction (OER), electrodeposition, electrochemical water splitting, electrocatalyst

Student Number: 2015-21045

Contents

List of Tables

List of Figures

Chapter 1. Introduction

1.1 Hydrogen as a Promising Renewable Energy Source

Since the global energy demand shows rapid expansion from last several decades, coping with serious environmental pollution and searching for new energy sources have been the pan-international problems. In the recent years, numerous researchers have shown great interest in exploring renewable energy conversion and storage system in order to appropriate increasing energy demands and prepare for depletion of fossil fuels. Fig. 1.1 shows global energy demand and energy generation by various energy sources. Among the various renewable energy sources, hydrogen is considered as a noticeable candidate, since hydrogen combustion does not discharge any air-pollutant. Unlike conventional fuel oil based energy sources, hydrogen is highly appreciated because of its carbon-neutral product as well as higher specific energy. Hydrogen is utilized as energy source in various sorts of fuel cells such as alkaline fuel cell (AFC), polymer electrolyte membrane fuel cell (PEMFC) and phosphoric acid fuel cell (PAFC). These diverse types of fuel cells are generally applied in vehicles and combined heat and power

(CHP) system. Hydrogen fuel has another advantage that typical hydrogen combustion system exhibits higher energy efficiency than hydrocarbon base fuel.

There are still many obstacles for hydrogen to alternate the existing fuels, however, mainly due to its difficulties in construction of efficient storage system and large-scale production. Originated from these abstruseness, a number of studies have been focused on developing efficient process of hydrogen production. Conventionally hydrogen gas is generated by the steam reforming of fossil fuels, which emits tremendous amount of carbon dioxide. Owing to the concerns on global warming, greenhouse gas-free photochemical, electrochemical and biological water splitting were suggested as alternatives. Fig. 1.2 displays simple outline of typical methods of hydrogen generation. Among suggested candidates, electrochemical water splitting has been spotlighted indebted with readily enlargeable process and high-purity hydrogen production.

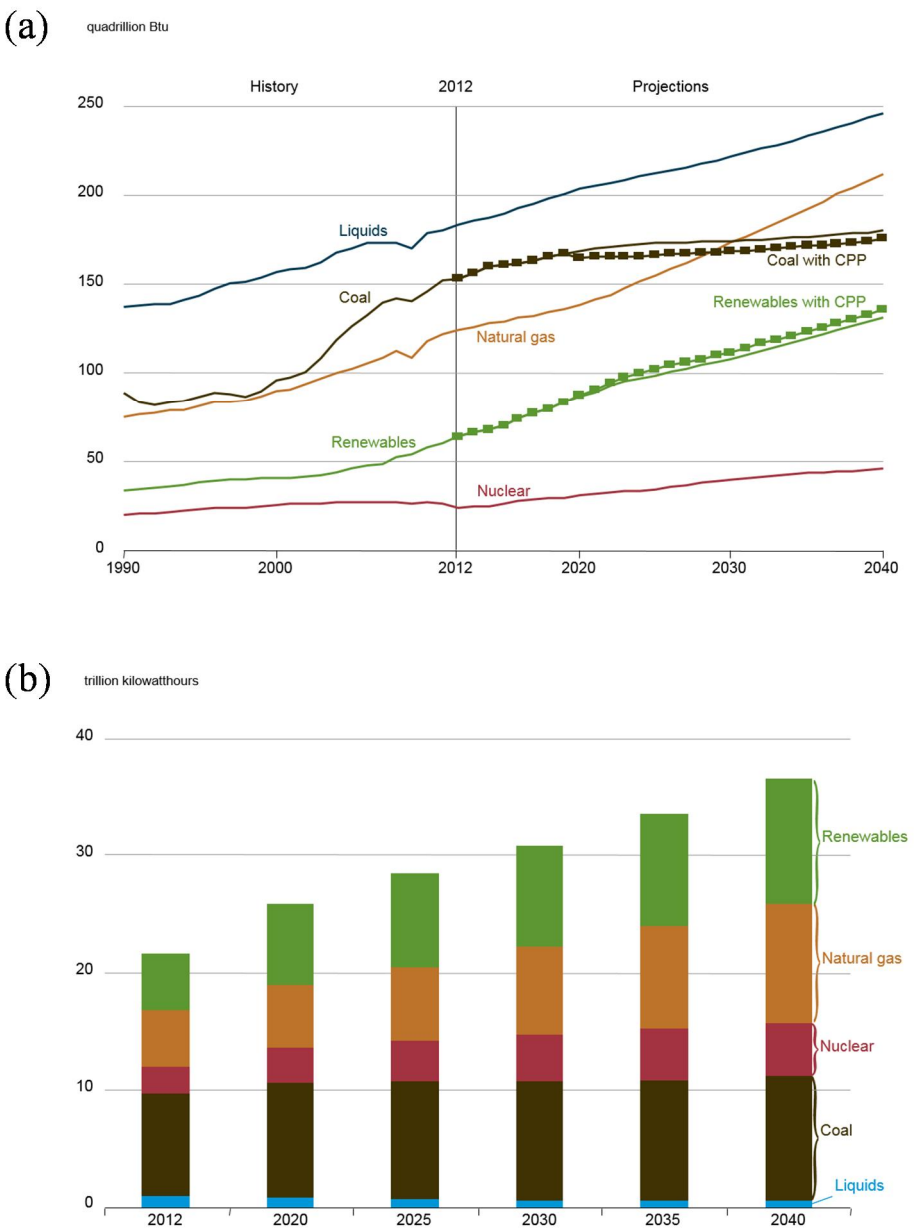

Fig. 1.1 (a) Global energy consumption by energy source, 1990~2040[1] and (b) Global electricity generation by energy source, 2012~2040.[1]

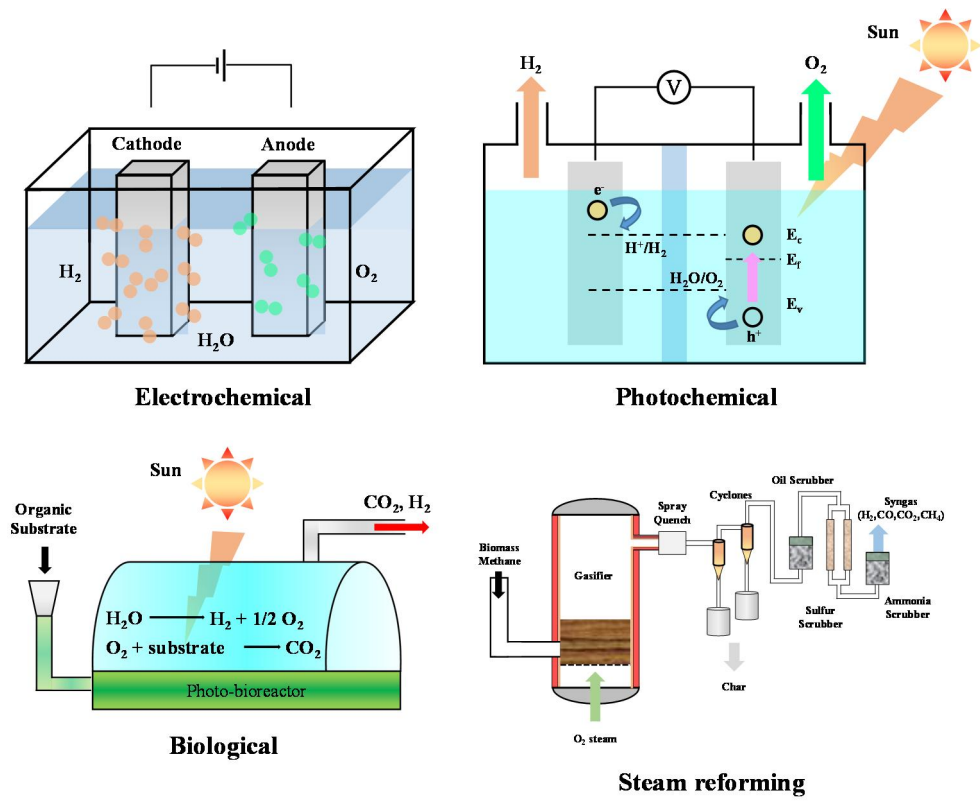

Fig. 1.2 Various methods of hydrogen production.

1.2 Electrochemical Water Splitting

Water is practically unlimited source of hydrogen on the earth, which only produces hydrogen and oxygen upon its splitting. Electrochemical water splitting deserves a great attention since it shows excellent efficiency to obtain hydrogen from water. The reactions for acidic and alkaline electrochemical water splitting on cathode and anode are given below.

In acidic,

Anode: $2H_2O \rightarrow 4H^+ + O_2 + 4e^-$ $E^0 = -1.23$ V (vs. NHE)

Cathode: $2H^+ + 2e^- \rightarrow H_2$ $E^0 = 0.00$ V (vs. NHE)

Overall: $2H_2O \rightarrow 2H_2 + O_2$ $E_{cell} = -1.23$ V (vs. NHE)

In alkaline,

Anode: $4OH^- \rightarrow 2H_2O + O_2 + 4e^-$ $E^0 = -0.40$ V (vs. NHE)

Cathode: $2H_2O + 2e^- \rightarrow H_2 + 2OH^-$ $E^0 = -0.83$ V (vs. NHE)

Overall: $2H_2O \rightarrow 2H_2 + O_2$ $E_{cell} = -1.23$ V (vs. NHE)

Fig. 1.3 reveals change in thermodynamic potential of each half reactions with pH. In alkaline media, 4 hydroxide ions are oxidized to form an oxygen and 2 water molecules at anode, while 2 water molecules are reduced generating a hydrogen and 2 hydroxides at cathode. Thermodynamic data of water splitting suggests that water splitting is an energy-required process. Incited with this, intensive investigations have been carried out to turn out efficient electrocatalysts for water splitting. Between two reactions on each electrodes, anodic reaction, usually called as the oxygen evolution reaction (OER), is thought to be rate-determining of overall water splitting since it involves 4 electrons, while the hydrogen evolution reaction (HER) includes only 2. Thus, OER usually requires much higher overpotential than HER. Fig. 1.4 shows the illustration of required potential to operate electrolytic cell assuming no Ohmic drop. Required potential for actual electrolysis is given as below.

$E_{applied} = E_{cell} + \eta_a + \eta_c + i(R_{solution} + R_{circuit} + R_{separator})$, where $E_{cell} = E_a^0 - E_c^0$

Required Energy = charge × voltage = $i \times t \times E_{applied}$

Production = charge × efficiency = $Q \times \sigma$(efficiency)

$E_{applied}$: Required potential for operation with current i

E_{cell}: Thermodynamic potential of cell

η_a/η_c: Overpotential of anode/cathode

i: Current

$R_{solution}$: Solution resistance

$R_{circuit}$: Circuit resistance

$R_{separator}$: Separator resistance

E_a^0/E_c^0: Anodic/cathodic half-cell potential

t: Time

Q: Charge

Ideally, potential difference of 1.23 V make water splitting possible in thermodynamically, however, it is not practical due to kinetic issues and internal resistance of the cell. Electrochemical reaction apparently occurs only when potential applied on electrode is above the thermodynamic cell potential. Overall energy required to manufacture same amount of production will decrease as the $E_{applied}$ is curtailed, because the production is practically independent of applied voltage. E_{cell} represents thermodynamic cell potential, which is already defined and there is no room for diminution. Ohmic drop induced by solution, circuit and separator resistance is also not related to electrodes. While on the other, η_a and η_c

indicate activation overpotential required to achieve certain amount of current density at anode and cathode, respectively. Net electrical current, which is approximately equivalent to reaction rate, increases exponentially as the overpotential increases when reaction was controlled by charge transfer. Equation describing such behavior, Butler-Volmer equation, is shown below.

$$i_{net} = i_0[e^{-\frac{\alpha F\eta}{RT}} - e^{\frac{(1-\alpha)F\eta}{RT}}]$$

i_{net}: Net current density

i_0: Exchange current density

α: Charge transfer coefficient

F: Faraday constant

R: Gas constant

T: Absolute temperature

In moderate overpotential region, it is assumed that mass transfer of reactant is sufficient, thus overpotential is sole parameter to determine current. This region is usually called as Tafel region. In Tafel region, anodic current becomes negligible

on cathode and vice versa for anode. Butler-Volmer equation is then simplified into Tafel equation by disregarding either former or latter one of right side. Tafel equation is shown as below for cathodic and anodic reaction.

Tafel equation: $\log|i_{net}| = \log i_0 - \frac{\alpha F\eta}{RT\ln 10}$ (cathodic)

or $\log|i_{net}| = \log i_0 + \frac{(1-\alpha)F\eta}{RT\ln 10}$ (anodic)

Tafel slope: $-\frac{\alpha_c F}{RT\ln 10}$ (cathodic) or $\frac{\alpha_a F}{RT\ln 10}$ (anodic)

Tafel plot, which typically shows linear relationship of $\log i_0$ vs η in the range of η > 118 mV is found by rearranging Tafel equation. Slope and intercept of Tafel plot attract attention since they explain kinetic feasibility and reversibility of the reaction, respectively. The slope of Tafel plot is termed as Tafel slope. Tafel slope serves as a criteria of how fast the charge is transferred between reactant and electrode. Catalyst with higher Tafel slope exhibits superior kinetic feature than others. Tafel slope is directly related to the mechanism and the rate determining step of electrochemical reaction. The general mechanism of OER is suggested in Fig. 1.5.[2-3] Under alkaline media, hydroxide ion binds to electrode surface releasing an electron. Then another hydroxide ion detaches hydrogen from adsorbed

hydroxide, remaining oxygen atom on the surface. In final step, bonding of two adjacent oxygen atoms produce single oxygen molecule. According to study of platinum anode at different current densities, electron transfer to hydroxide (step 3 of Fig. 1.5 (b)) or hydroxide adsorption (step 1 of Fig. 1.5 (b)) may serve as the rate determining step.

As mentioned above, overall efficiency of the electrolysis is referred as σ. This is called as Faradaic efficiency or Coulombic efficiency, defined as the ratio of actual production to theoretical production. 100% of Faradaic efficiency indicates perfect conversion of consumed charge to product, which may not achieved when electrolyte decomposition, surface deterioration or side reaction is accompanied by. Side reaction and electrolyte decomposition are often negligible in water splitting system since typical electrolyte contains mostly strong acid or base solely with inert counter ions, while surface degeneration may significantly reduce Faradaic efficiency as the electrode suffers oxidation, detachment, dissolution of components or loss of crystallinity during the operation.[4] System without such problems generates product as the equivalent amount of applied charge. Faradaic efficiency of water splitting is commonly estimated with gas chromatography (GC), since both products exist as gaseous phase in general operation condition.

For large-scale application, long-term stability need to be considered as another

great issue. Problems that earlier mentioned as reasons of efficiency decrease may also considerably decrease durability of catalyst. For instance, dissolution of catalyst material might induce unwanted side reactions on both electrodes as well as decreased catalytic activity. Therefore, sustained activity of catalysts upon prolonged working must be confirmed for practical use.

Among the all sorts of electrocatalysts, platinum is already known as one of the most efficient catalyst for hydrogen production, while iridium oxide and ruthenium oxide are ranked as the uppermost standard for OER.[5-8] Excellent catalytic behavior on OER of iridium oxide and its kinetic mechanism are already known over last several decades.. S. Gottesfeld et al. earlier explained the role of oxide formation on Ir electrode for oxygen evolution.[9] Oxide layer provides positive polarization on metal ion, which leads rapider oxygen adsorption. Such behavior was described in terms of higher Tafel slope, indicated in Fig. 1.6 (b). These catalysts have ultimate disadvantages; nevertheless, extremely high prices of precious metals such as platinum, iridium or ruthenium limit their usage on the mass production of hydrogen. This demerit inspired many researchers to exert efforts for substitution of noble metals to cheaper ones. Since the cost of electrochemical water splitting is strongly related to the overpotential of OER on anode and expenditure on catalysts, it is essential to develop cost-effective and highly active electrocatalyst to promote

OER.

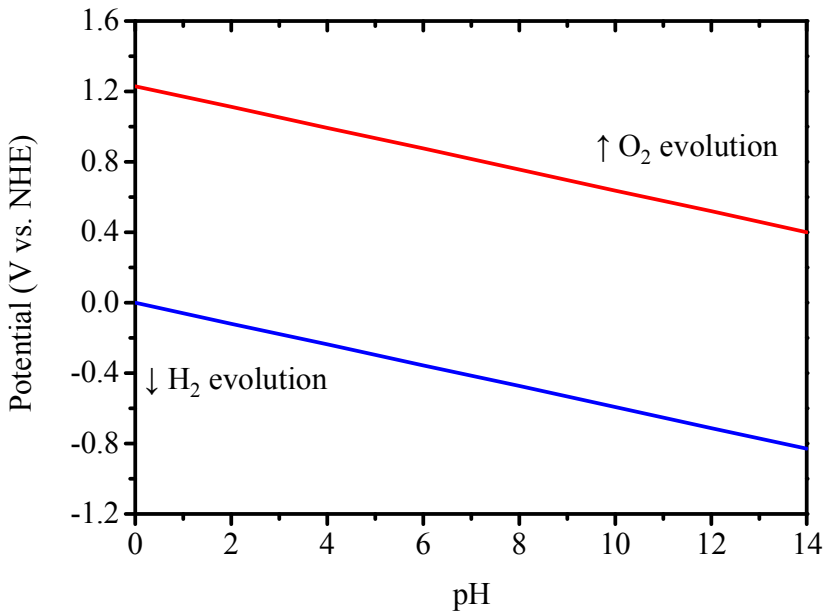

Fig. 1.3 Thermodynamic potential of oxygen evolution and hydrogen evolution upon pH change.

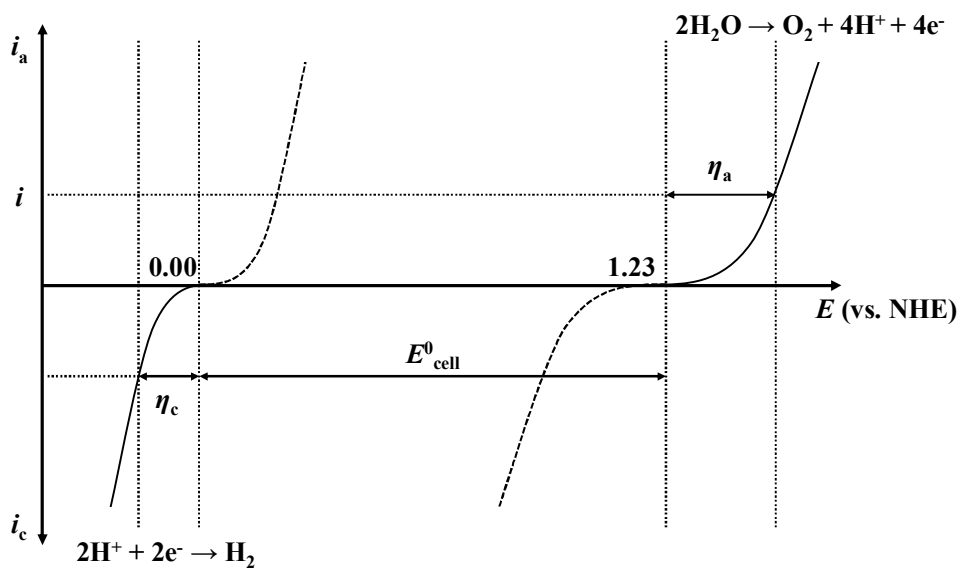

Fig. 1.4 Working voltage of Ohmic-drop-free water splitting cell.

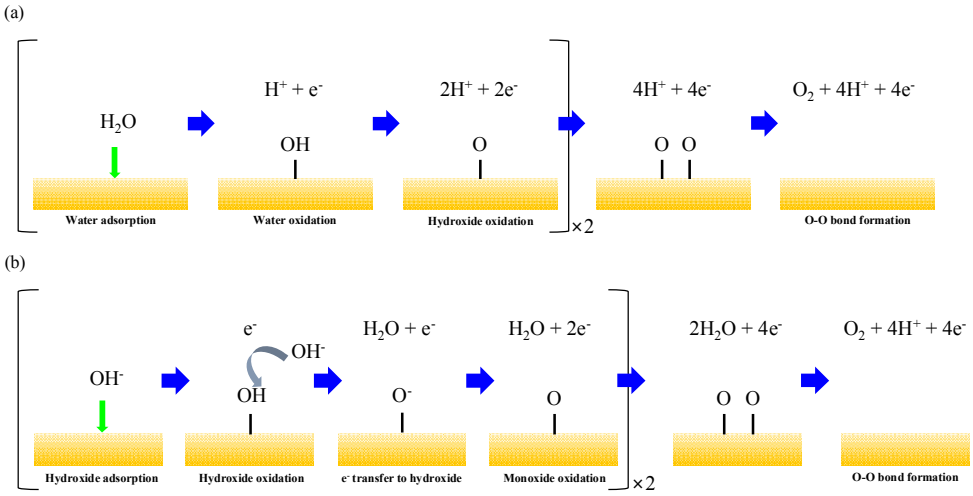

Fig. 1.5 General mechanism of oxygen evolution reaction in (a) acidic and (b) alkaline media.[2-3]

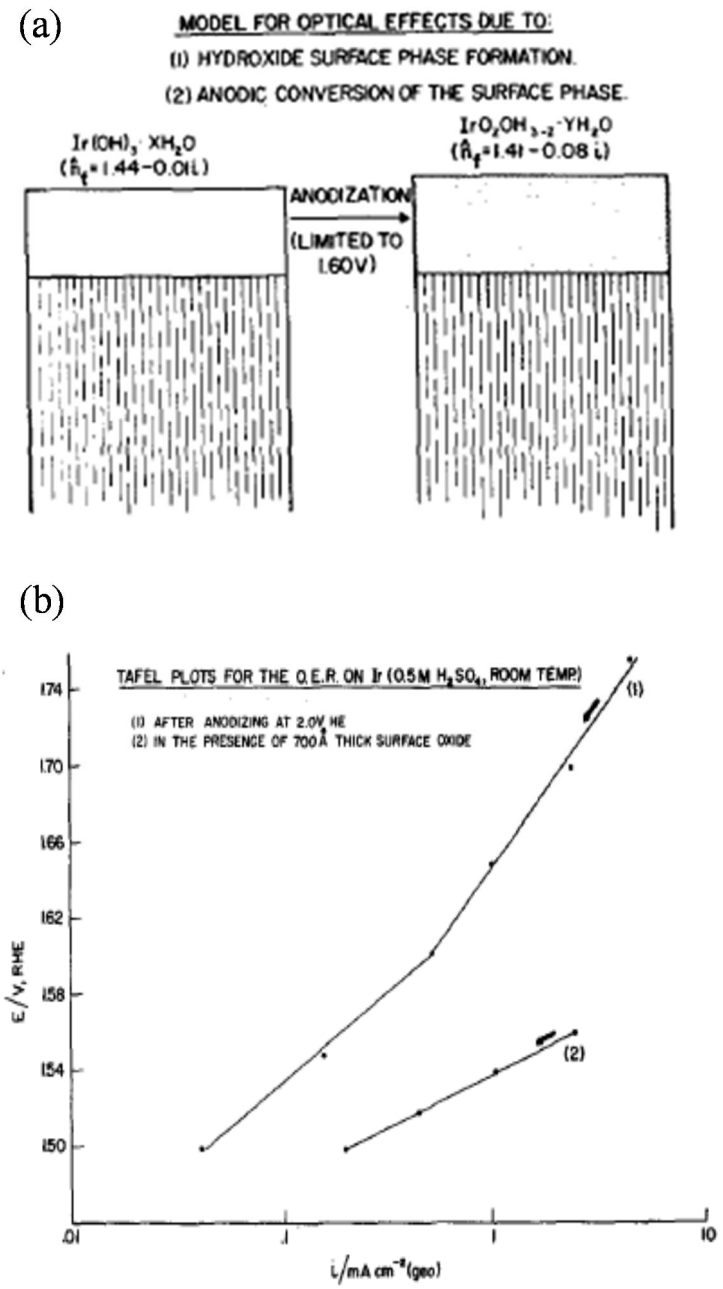

Fig. 1.6 (a) Schematic presentation of Ir hydroxide formation by potential multicycling and its anodic conversion and (b) Tafel plots for the OER on Ir (1) in the absence of the thick phase oxide; (2) in the presence of phase oxide.[9]

1.3 Transition-metal-based Catalysts and their Alloys for Water Oxidation

Recently, many researches were focused on transition-metal-based catalysts because of their low cost, good stability and high catalytic activity on OER. Not only transition metals, but also many derivatives such as phosphorous-alloy-based, sulfides, layered double hydroxides (LDHs), carbides, selenides and oxides have been suggested as promising catalysts. Up to the present, NiO_x[10], CoO_x[11], $NiCoO_x$[12], NiFe/NF[13], Ni/Fe[14] and Ni/V LDH[15], Ni_2P[16], Co-P[17], Ni-P/CF[18], Ni-P/NF[19] and Ni_2P nanoparticles[20] were representatively reported for efficient OER catalysts. Table 1.1 compares the properties of various catalysts listed ahead. As shown in the list of previously reported catalysts, first-row late transition metals are especially attracted much attention, due to their abundance. Nickel and nickel-based materials were exceptionally often applied for water splitting electrocatalyst owing to its high catalytic activity. Popczun et al. early investigated nano-structured nickel phosphide (Ni_2P) as an extraordinarily active and stable for HER.[21] Although primarily nickel phosphorous derivatives were introduced as excellent HER catalysts, application on OER catalysts of nickel-based materials

has been attempted lately. Wang et al. fabricated self-supported porous nickel phosphide foam for application on overall water splitting.[19] Stern et al. recently showed a Ni_2P nanoparticles, which is already known as prominent HER catalyst, exhibits high OER activity resulting from the core-shell nickel phosphide/nickel oxide (Ni_2P/NiO_x) structure of nanoparticle.[20] Liu et al. reported electrodeposited nickel-phosphorous nanoparticle film as a bifunctional electrocatalyst for efficient water electrolysis.[18]

Coupled with transition-metal-based promising electrocatalysts, many attempts have been made to further enhance catalytic activities with adding another metal in existing catalysts. Variety of combinations such as Ni/Fe[11], Co/Fe[11], Ni/Co[12], Ni/Ce[10], Ni/La[10], Ni/V[15] have been suggested so far. These alloy catalysts often deliver higher catalytic activity than separated single-metal-based ones, due to synergetic effects induced by transition of valence state and enhanced electrical conductivity. Many researchers thus are trying to discover unprecedented, suitable combinations for excellent OER catalysts application.

Table 1.1 Examples of Recently Reported First-row Transition Metal OER Electrocatalysts

Catalyst	Preparation method	substrate	Ref
NiO_x	electrodeposition	Ni	10
CoO_x	electrodeposition	Pt	11
$NiCoO_x$	electrodeposition	Cu	12
NiFe/NF	electrodeposition	Ni foam	13
Ni/Fe LDH	hydrolysis + thermal treatment	MW CNTs	14
Co-P	electrodeposition	Cu	17
Ni_2P	thermal reaction	GC	16
Ni-P/CF	electrodeposition	Cu foam	18
Ni-P/NF	thermal vapor phosphorization	Ni foam	19
Ni_2P NPs	thermal reaction	Ni	20

1.4 Electrodeposition for Application in OER Electrocatalyst

Electrodeposition (electroplating) is a process which prepares metal or metal alloy coating with the assistance of external electrical current. Purposes of electrodeposition includes forming electrical interconnection, application of catalysts, protection (passivation) of surface, enhancement of mechanical and chemical properties or decoration. Generally, electrodeposition is carried out in the electrochemical cell consisting of electrodes, electrolyte containing metal ion to be deposited and some sort of additives (if required). Fig. 1.7 displays typical scheme of electrodeposition. Electron supply at cathode enables metal deposition.

Most of reported OER catalysts have given emphasis on nanostructure holding high surface area.[13,18-20,22] These catalysts usually assume the form of powders, which require conductive adhesive polymers to be applied on electrode surface. Such process may reduce active surface area and electrical conductivity considerably, resulting in decreased catalytic activity. Poor adhesion properties especially on high current condition is another point to be considered. Electrodeposition enables formation of smooth and highly uniform surface with excellent adhesion, gaining advantage of application assisted by polymeric binder. Another strong advantage of electrodeposition is its relative convenience on

industrial, large-scale application, exemplified by the semiconductor processes. From a practical viewpoint, feasibility for mass production made electrodeposition as promising candidate for preparing electrocatalysts.

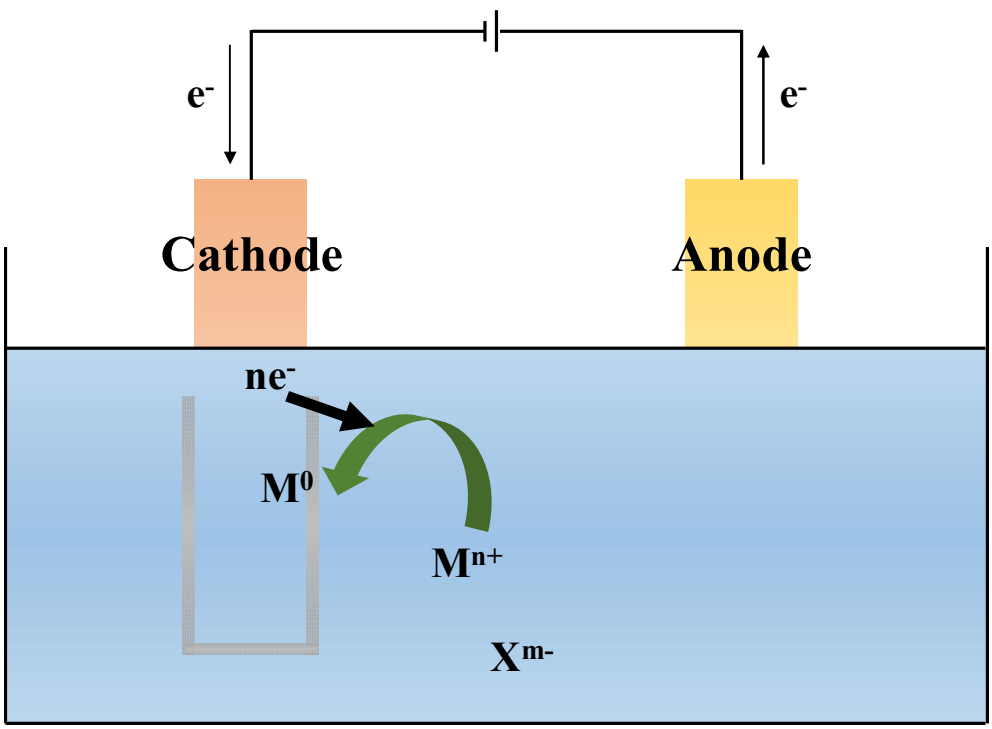

Fig. 1.7 General scheme of metal electrodeposition.

1.5 Purpose of the Study

As electrocatalysts exhibiting high OER activity have attracted great attention, numerous kinds of catalysts have been reported. Among them, electrodeposited transition metal catalysts have diverse merits for large-quantity production as aforementioned. This study discusses electrodeposited nickel-copper phosphorous catalyst and its application on OER electrocatalyst. While nickel has taken great attention on water splitting electrocatalysts recently, its application in hydrogenation and hydrogenolysis have already been industrialized in hydrocarbon reforming processes.[23] In connection with this, numerous of studies have attempted to improve catalytic activity of nickel-based catalysts with addition of other metals.

Copper has been suggested as one of alloying candidate, since it has similar lattice parameters (3.61 Å) with nickel (3.51 Å) and forms continuous binary solid solution with nickel below 1085℃. Fig. 1.8 illustrates phase diagram of nickel-copper binary system. Earlier, interaction between nickel and copper in solid solution has been reported with various XRD and XPS studies, which eventually confirmed that catalytic activity change of solid solution is related to the degree of alloying. Earlier Hufner et al. described correlation between density of states based on XPS and calculated band structures.[24] Naghash et al. has revealed that change of

catalytic activity is related with transition on electronic state of nickel, which is also confirmed by XPS studies.[25] According to this study, binding energy of Ni $2p_{3/2}$ has shifted toward positive direction with addition of copper. Although nickel-copper alloy does not always enhance the catalytic activity of certain reaction, it is noticeable since it may enable further enhancement of electrocatalyst activity containing nickel. Many studies of metal-phosphorous based catalysts already found that phosphorous content causes betterment of their activities by inducing partial positive charge on active metal centres.[16-17,20] The background of enhanced activity was found earlier with comparing surface XPS analyzes of Ni and NiP.[20] When Ni serves as an OER catalyst, surface of Ni oxidizes to NiO, and then further oxidized to $Ni(OH)_x$ species. Thus, in general, outermost $Ni(OH)_x$ species are directly responsible for OER activity. Thermodynamically unstable properties of oxyhydroxides, however, decreases stability of the layer.[26] Supporting ability of $Ni(OH)_x$ layer was enhanced for phosphorous containing case, compared to $Ni/NiO/Ni(OH)_x$ supporting layers, which is revealed by clearly increased activity.[20] Indebted to this, it was expected that blending copper on nickel-based catalyst also has potentiality to bring out additional increase of catalytic activity.

From the viewpoint of facile production, electrodeposition was chosen as an appropriate method, due to its simple procedure. Moreover, while many metal

catalysts requires high temperature and long time for their fabrication, electrodeposition often does not. Electrodeposition directly coats catalyst material on the substrate in a short time with excellent adhesion. Electrodeposition of metal often requires complexing agent in order to achieve sufficient control on deposition current, which allows building on high quality film. When complexing agent forms complex with metal, reduction of metal ion occurs on more negative potential because metal ion becomes thermodynamically more stable in the electrolyte. Coordination of metal ion thus practically reduces deposition rate, which allows feasibly controlled metal deposition without formation of undesired poor-adhesive structure such as dendrite or whisker. Ethylenediamine (EN), which is already widely known as strong metal-chelating agent, is introduced in this study since formation constant (K_f) of $Cu(en)_3^{2+}$ overrides that of $Ni(en)_3^{2+}$ complex. This means difference in deposition potential between nickel (-0.23 V vs. NHE) and copper (+0.34 V vs. NHE) decreases as a consequence of complex formation. Table 1.2 indicates formation constants of typically used complexing ligands. Electrodeposition of phosphorous alloy is generally achieved with addition of sodium hypophosphite ($Na_2H_2PO_2$) in the electrolyte. Main reactions of phosphorous addition is expressed by following equations.

$$H_2PO_2^-(aq) \rightarrow H_2PO_2^-(ads)$$

$$H_2PO_2^-(ads) \rightarrow H\dot{P}O_2^-(ads) + \dot{H}(ads)$$

$$H_2PO_2^-(aq) + H^+(aq) \leftrightarrow H_3PO_2(aq)$$

$$H_3PO_2(aq) + \dot{H}(ads) \rightarrow P(s) + H_2O(l)$$

Precautions should be taken since sodium hypophosphite is also used as the reducing agent of electroless copper or nickel deposition system.[27] In this study, occurrence of electroless deposition by sodium hypophosphite can be restricted in ambient condition, however, since ethylenediamine serves as strong complexing agent limiting electroless deposition of nickel and copper within only negligible level.

Table 1.2 Formation Constants of Several Complexing Agents of Nickel or Copper Coordinated Compounds[29]

K_f (25℃)	Ni^{2+}	Cu^{2+}
CN^-	2.0×10^{31}	3.8×10^{18}
EDTA	3.8×10^{18}	5.0×10^{18}
EN	2.1×10^{18}	1.1×10^{20}
NH_3	5.5×10^{8}	1.1×10^{13}
oxalate	3.0×10^{8}	3.0×10^{8}

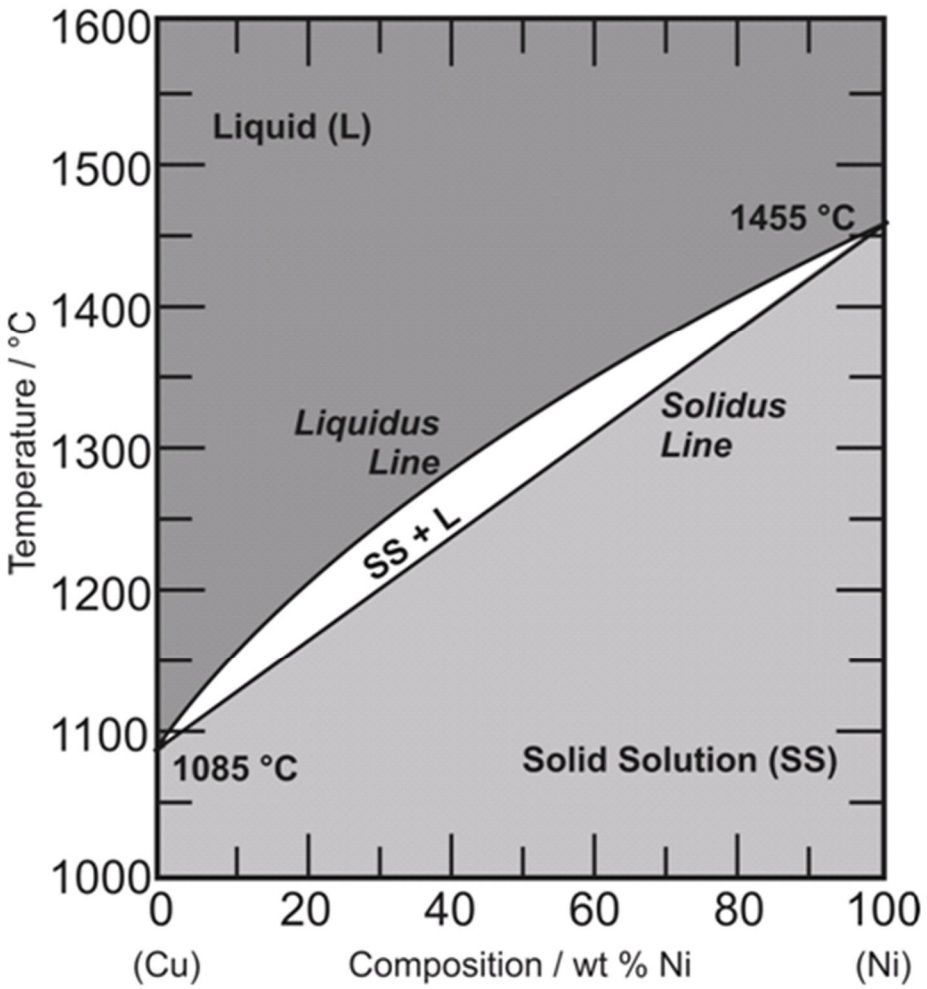
1600
1500
1400
1300
1200
1100
1000
Temperature / °C
Liquid (L)
1455 °C
Liquidus
Line
Solidus
Line
SS + L
1085 °C
Solid Solution (SS)
0
20
40
60
80
100
(Cu)
Composition / wt % Ni
(Ni)

Fig. 1.8 Binary phase diagram of nickel-copper alloy.[28]

Chapter 2. Experimental

2.1 Preparation of Catalyst

Copper rotating disk electrode (RDE) or foil (Alfa Aesar) was used as substrate in this study. Geometric area of Cu RDE was 0.1257 cm^2 (4 mm diameter). Cu foil was pasted on glassy carbon (GC) electrode with silver conductive adhesive, then exposed area was also fixed as 0.1257 cm^2. Pt wire and saturated calomel electrode (SCE) were used as counter and reference electrode, respectively. Cu electrode was firstly washed with absolute ethanol then rinsed with deionized water to remove organic residues. For native oxide removal, cyclic voltammetry on 0.0 V ~ -1.5 V (vs. SCE) was cycled for 5 times in 0.1 M citric acid solution with 50 mV/s scan rate and 1500 rpm rotation speed. After oxide removal, DI water was used to cleanse residual citric acid. The solution for Ni-Cu phosphorous electrodeposition was prepared with $CuSO_4 \cdot 6H_2O$, $NiSO_4 \cdot 6H_2O$, ethylenediamine and KOH. All of materials in preparing solution were purchased from Sigma Aldrich. In order to confirm the effect of Cu content on catalyst, ratio of Ni/Cu was varied in the solution. Detailed compositions of the solution were presented in Table 2.1.

Preparing solution was purged for 20 min with N_2 gas to remove dissolved gas in the solution. When constant potential was applied for electrodeposition, variation of initial current on each experiment resulted in poor reproducibility. Thus, electrodeposition was carried out with two-step preparation method. -8 mA of constant current was applied for 1 s in the first step and then constant potential of -1.711 V (vs. SCE) was applied until the total charge reaches 20 C/cm^2. RDE was rotated with 1500 rpm to remove hydrogen gas during the deposition. After electrodeposition, the catalyst electrode was immediately removed from the solution then rinsed with DI water. The catalyst then went through electrochemical measurement or stored in vacuum chamber for further analysis.

Table 2.1 Compositions of Solution for Ni-Cu Phosphorous Electrodeposition

Nomenclature	NiP	NiCuP**9991**	NiCuP**4991**	NiCuP**1991**	NiCuP**991**	NiCuP**491**
Ni/Cu ratio	Ni only	999 : 1	499 : 1	199 : 1	99 : 1	49 : 1
						Total $[Ni^{2+}] + [Cu^{2+}] = 50$ mM
NaH_2PO_2	0.500 M					
en	0.150 M					

2.2 Electrochemical Measurements

The standard three-electrode electrochemical cell was used to perform electrochemical analyses. Cu RDE or pasted foil and saturated calomel electrode (SCE) were also used as working and reference electrode, respectively. For activity comparison of Ni and NiP, Ni RDE was used instead. All of electrochemical measurements were recorded with PATSTAT™ MC Potentiostat (Princeton Applied Research). Potentials were firstly recorded vs. SCE then converted to vs. reversible hydrogen electrode (RHE) using equation $E_{(RHE)} = E_{(SCE)} + 0.242 + 0.05916 \times pH$. Pt wire was used as a counter electrode.

Polarization curves were obtained in strong KOH solution (pH = 14) from 0.3 V ~ 0.7 V (vs. SCE) with 2 mV/s scan rate. 2000 rpm of rotation was applied during the voltammetry to remove evolved oxygen. Uncompensated resistance (R_u) was determined then compensated for 95% level during the measurement in order to correct the Ohmic drop. IR compensated polarization curves were directly used for comparing OER performance. Electrochemical surface area (ECSA) was measured for each catalyst with cyclic voltammetry (CV) on potential range of 0.05 V → -0.05 V (vs. OCP) with 2, 5, 10, 25, 50, 100 and 200 mV/s scan rates for 5 cycles. Potential was held for 10 s at each vertex potential. Non-Faradaic current on each

vertex potential was plotted against the scan rate, obtaining double layer charging capacitance (C_{dl}) from slope of the plot. Chronopotentiometry (CP) was carried out for evaluating long-term stability of catalyst. 18 hours of operation was performed in pH 14 KOH solution with 2000 rpm rotation. Current density of CP was maintained as 10 mA/cm^2.

Potentiostatic electrochemical impedance spectroscopy (EIS) was performed for measuring charge transfer resistance (R_{ct}) of catalysts. Real and imaginary impedance components were recorded with Potentiostat between 100 kHz and 0.1 Hz with 10 mV amplitude scale. Potential was set as 0.6 V (vs. SCE), which corresponds to 377 mV overpotential. Nyquist plot was obtained with plotting imaginary components against real parts of measured impedance. In order to calculate R_{ct}, minimum frequency was curtailed as 100 Hz for excluding mass transfer controlled region.

2.3 Gas Chromatography Measurements

Evolved oxygen gas was detected with gas chromatograph (SERIES II Plus 5890, Hewlett Packard) coupled with electrochemical cell connected to Potentiostat. Electrochemical experiments were conducted in a gas-tight homemade cell. Fig. 2.1 indicates scheme of cell configuration. 20 psi of 99.999% He was used as a carrier gas during the experiment. Before electrochemical experiments, 30 min of purging with 100 ccm 99.999% N_2 was executed for removal of dissolved oxygen in electrolyte. N_2 blowing was maintained during the experiment with 100 ccm. Flow rate of inlet and outlet of the cell was confirmed to be fixed with gas collection over water. Fresh air went through GC firstly and then chromatogram was recorded for setting calibration standard (volumetric proportion of oxygen in fresh air, 20.95%). 10 mA of constant current was applied throughout the experiment. After initiation of applying current, gas sample was injected in no time into the column in every 3 min, and was repeated up to total experiment duration reached 51 min. Magnetic stirrer was used to stirring the electrolyte for amicable exhaust of evolved gas. The measurement was performed with thermal conductivity detector (TCD) inside of the instrument. Amount of measured gas was calculated with accumulating generated oxygen by assuming constant generation

rate during each 3 min period. Ideal O_2 production (assumed 100% Faradaic efficiency) was calculated with following relation.

$$10\ \text{mA} = 10\,\frac{\text{mC}}{s} = \frac{10^{-2}\ C/s}{96485\ C/eq \times 4\ eq/mol} = 2.591 \times 10^{-8}\ mol/s$$

Volumetric fraction of evolved oxygen is then calculated with ideal gas law, then compared to standard peak (oxygen peak of fresh air). Faradaic efficiency was calculated with dividing measured generation rate by theoretical generation rate.

$$\text{Faraidac Efficiency (FE)} = \frac{Measured\ (actual) generation}{Theoretical\ (calculated)\ generation} \times 100\%$$

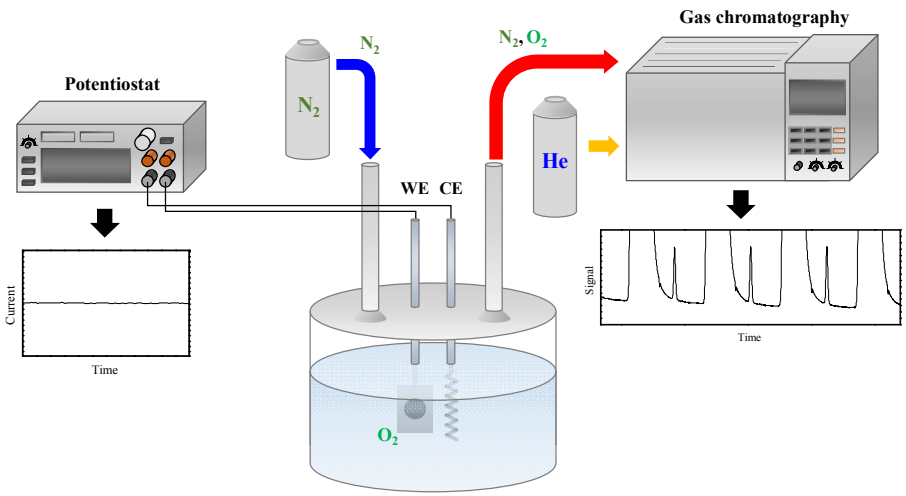

Fig. 2.1 Schematic illustration of gas chromatography experiment.

2.4 Characterization of Catalyst

Surface morphology and elemental composition of prepared catalyst were investigated using field-emission scanning electron microscopy (FE-SEM) and energy-dispersive X-ray spectroscopy (EDS, MERLIN Compact, ZEISS), respectively. X-ray photoelectron spectroscopy (XPS) measurements were conducted on ESCA Sigma Probe from VG Scientific with Al anode. Observed XPS spectra was calibrated with C 1s peak (binding energy 284.8 eV). Phase composition of prepared catalysts were examined by X-ray diffraction (XRD, D-8 Advance, BRUKER MILLER Co.) patterns. Scanning range was set as from 40˚ to 80˚ with 2˚ /min scan rate.

Chapter 3. Results and Discussion

3.1 Optimization of Preparation Conditions

Prior to electrodeposition, determining preparation potential is essential step to obtain high-quality catalyst surface. Difference in reduction potential of nickel and copper makes it attentive to set deposition potential. Fig. 3.1 (a) indicates linear sweep voltammetry (LSV) with 50 mV/s scan rate in electrolyte containing different ratio of nickel and copper. Composition of electrolyte is identical with above mentioned catalyst preparing solution with varying the ratio of nickel and copper lies between 4~0.25. Ratio in legend explains proportion of Ni^{2+}:Cu^{2+}. Experimental results illustrates that Cu deposition starts +0.28 V (vs. RHE) while Ni deposition commences at -0.30 V (vs. RHE). Cu deposition typically shows limiting current when overpotential sufficiently increases, as explained by Levich equation below.

$$i_{l,c} = \frac{0.62nFAD_o^{2/3}C_0^*\omega^{1/2}}{\nu^{1/6}}$$

$i_{l,c}$: Cathodic limiting current

n: Number of electron involved in the reaction

A: Surface area

D_0: Diffusion coefficient

C_0^*: Initial bulk concentration

ω: rotation speed

ν: Kinematic viscosity

Since limiting current is proportional to bulk concentration of reductive species, linear relationship between must be confirmed when plotting $i_{l,c}$ vs C_0^*. Fig. 3.1 (b) elucidates such behavior. Mass-limiting currents of Cu were found on below -0.2 V, which corresponds to ~500 mV of overpotential. Deposition potential on this study was set as -0.8 V (vs. RHE) since in higher overpotential region, hydrogen evolution during the preparation is too severe, resulting in high fluctuation on deposition current profile. In lower overpotential region, catalytic activity was lower than that of -0.8 V.

Violent hydrogen evolution is accompanied by catalyst deposition on the working electrode because of negative deposition potential. Evolved hydrogen thus

blocks the electrode surface as deposition proceeds. Flushing out generated hydrogen is required, therefore, and it is achieved by rotating working electrode at a great speed. Applying less than 1000 rpm rotation resulted in inefficient removal of evolving gas, thus deposition profile fluctuated significantly. When applying rotation of 1500 rpm or above, produced catalysts exhibited almost similar activities. Hence 1500 rpm rotation was applied for the experiment.

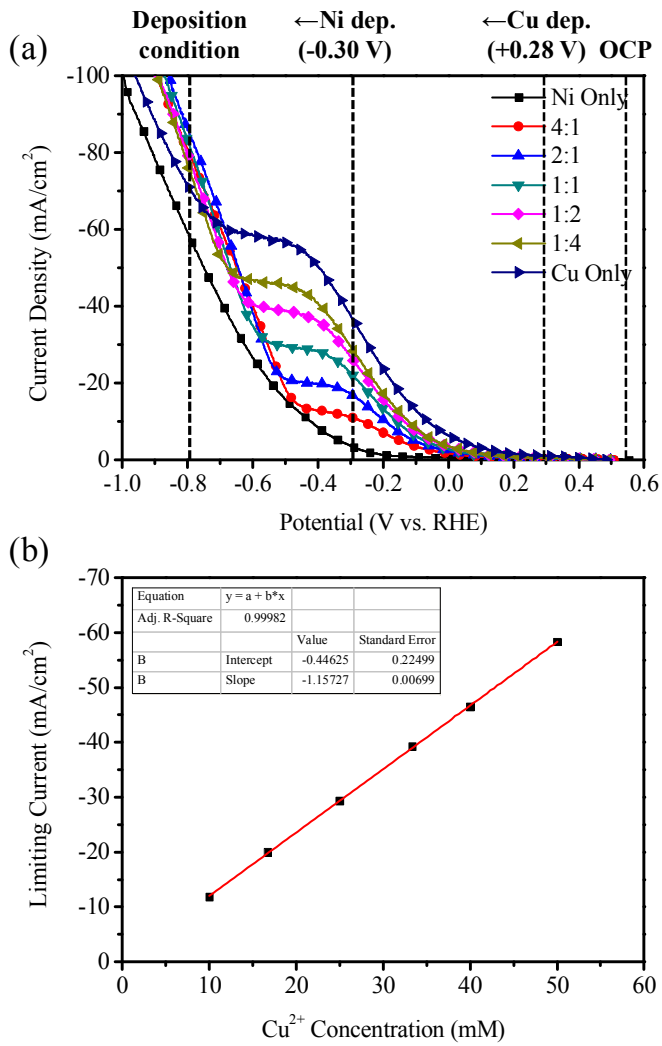

Fig. 3.1 (a) Current profiles of LSV in electrolytes containing 4:1, 2:1, 1:1, 1:2 and 1:4 (Total $[Ni^{2+}] + [Cu^{2+}] = 50$ mM) ratio of Ni^{2+} : Cu^{2+} and containing 50 mM of Ni or Cu only and (b) Plot of limiting current vs Cu^{2+} concentration.

3.2 Optimization of Catalyst Composition

Naturally Ni itself exhibits catalytic activity toward OER, it is already mentioned that phosphorous content further enhances the activity. Polarization curves of Ni RDE and electrodeposited NiP are shown in Fig. 3.2, which reveal obvious enhancement of catalytic activity. Tafel slope of NiP also decreased up to 51.8 mV/dec, while Ni only shows 75.3 mV/dec. For further experiments, therefore, phosphorous was regarded as essential composition to prepare highly active catalysts.

When polarization curves are obtained from open circuit potential (OCP) toward high positive potential, oxidation peaks appear around 0.35 V and 1.40 V. Black line with square symbol in Fig. 3.3 (a) indicates such behavior. These oxidation peaks can be assigned as Ni oxidation to NiO (Ni^{2+}) and further oxidation of NiO to NiOOH (Ni^{3+}), respectively. Unlike HER Ni catalysts, many previous reports of OER Ni catalysts suggest this pre-activation step.[18-20, 30] Ni experiences surface oxidation during the polarization in the initial stage, then activity increases significantly. It is also known that outermost NiOOH layer are directly responsible for OER catalytic activity. Repetition of polarization curves indicates gradual increase in activity and OCP, then remain same after 5 cycles. Clearly increased

activity of 5th cycle in Fig. 3.3 (a) demonstrates importance of pre-activation step. In order to consult convenience, 5th cycle was expressed as suggested polarization curve hereafter.

Various ratios of Ni/Cu were applied in order to trace out optimized proportion. Polarization curves of deposits prepared by multiple ratios of Ni/Cu in electrolyte were illustrated in Fig. 3.3 (b) and (c). Noticeable fact is that NiCuP991 and NiCuP1991 showed best performance toward OER among various ratios. It is also worth mentioning that although NiCuP11 indicates higher activity than NiP, it may simply due to higher surface area induced by mass transfer limited deposition of high concentration Cu (see Fig. 3.4 and Fig. 3.5), supported by extreme high current density in below 1.50 V. Tafel plot was obtained from $\log i$ vs η plotting, as indicated in Fig. 3.3 (d) while slopes of linear relationship between $\log i$ and η (Tafel slope) were presented in Fig. 3.3 (e). Among various catalysts, NiCuP1991 showed best kinetics for OER (42.5 mV/dec). As Cu content increases, Tafel slope tend to decrease up to the Ni/Cu ratio 199:1, while additional increase turns slope toward rising trend. In summary, assumed optimized ratio of Ni/Cu is 199:1. Fig. 3.3 (b) still remains question, however, that although NiCuP1991 exhibits lower Tafel slope, apparent activity was higher for NiCuP991. Since NiCuP11 showed exceptionally high charging current under non-Faradaic region, Cu content increase

might induced increment of surface area. Hence, it was speculated that high surface area of NiCuP991 might exaggerated catalytic activity.

Electrochemical surface area (ECSA) was measured to compare surface area of catalysts by estimating double-layer charging capacitance (C_{dl}) with cyclic voltammetry. Small currents observed in non-Faradaic potential region often used for this experiment. After voltammogram became stable, maximum anodic and cathodic current (i_0) were plotted against scan rate. Fig. 3.4 (a) shows typical voltammogram of 5th cycle of NiCuP1991. Slope of i_0 vs ν plot then directly corresponds to C_{dl} value. ECSA is estimated with dividing C_{dl} by specific capacitance (C_s) of the substrate assuming planar surface. In strong alkaline media, general specific capacitances lie between C_s = 0.022~0.130 mF/cm^2.[31] In this study, C_s = 0.050 mF/cm^2 was used as the reference of C_s value. Fig. 3.4 (b) represents i_0 vs ν plot of NiCuP1991 for both anodic and cathodic currents. For NiCuP1991, C_{dl} = 0.118 (± 0.00279) mF/cm^2 was obtained for capacitance, which corresponds to 2.36 (± 0.137) /cm^2 ECSA. This implies that surface area of NiCuP1991 is about 2.36 times higher than nearly ideal smooth surface in alkaline solution. C_{dl} and ECSA values for other catalysts were also calculated and then shown in Fig. 3.4 (c). Generally, surface area of NiCuP4991 and NiCuP1991 did not show considerable difference compared to that of NiP. When Ni/Cu ratio reaches higher than 99:1,

however, significant increase in surface area was observed. Note that C_{dl} of NiCuP991 was calculated as 0.290 (± 0.0246) mF/cm^2. C_{dl} of catalyst with higher Cu content than NiCuP991 increases even more rapidly.

In order to compare the catalytic activity with excluding effect of surface area, "normalized" polarization curve was obtained in Fig. 3.4 (d). This curves were calculated based on the assumption that surface area of each catalyst is equivalent to that of NiP. As shown in the Fig. 3.4 (d), NiCuP1991 exhibited the best OER performance per unit area. The reason of higher catalytic activity of NiCuP991 than NiCuP1991 was therefore turned to be due to 2.46 times higher surface area. Normalized activity was increased up to 199:1 Ni/Cu ratio, then diminished with further Cu addition, which is also in accord with the tendency of Tafel slope (Fig. 3.3 (e)). Fig. 3.5 (a) indicates Tafel plot obtained from polarization curve with normalization (Fig. 3.4 (d)). After normalization, exchange current density (i_0) was calculated for each catalyst with intercept of Tafel plot. As found in Fig. 3.5 (b), NiCuP1991 showed superior exchange current density compared with other catalysts. In short, NiCuP1991 was considered as the best OER electrocatalyst among the candidates.

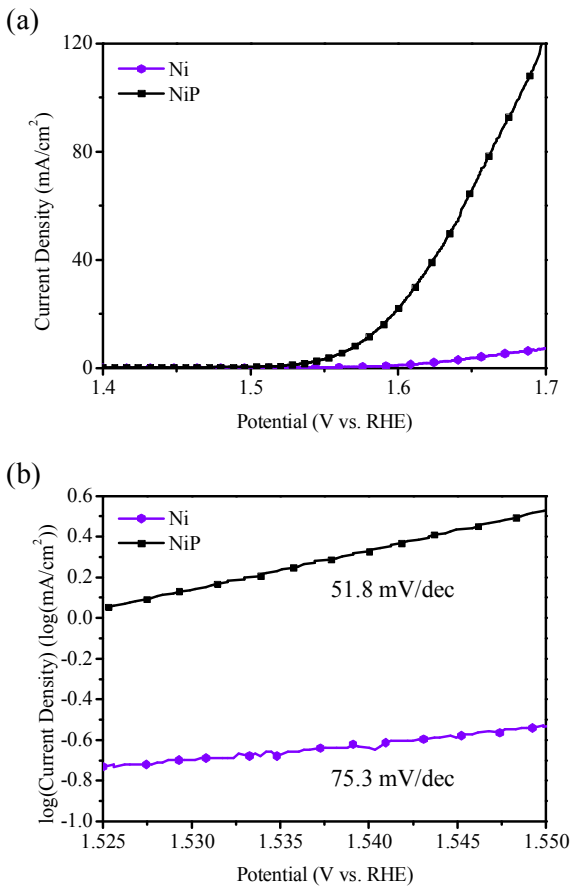

Fig. 3.2 Comparison of OER activity between Ni and NiP (a) polarization curve and (b) Tafel plot.

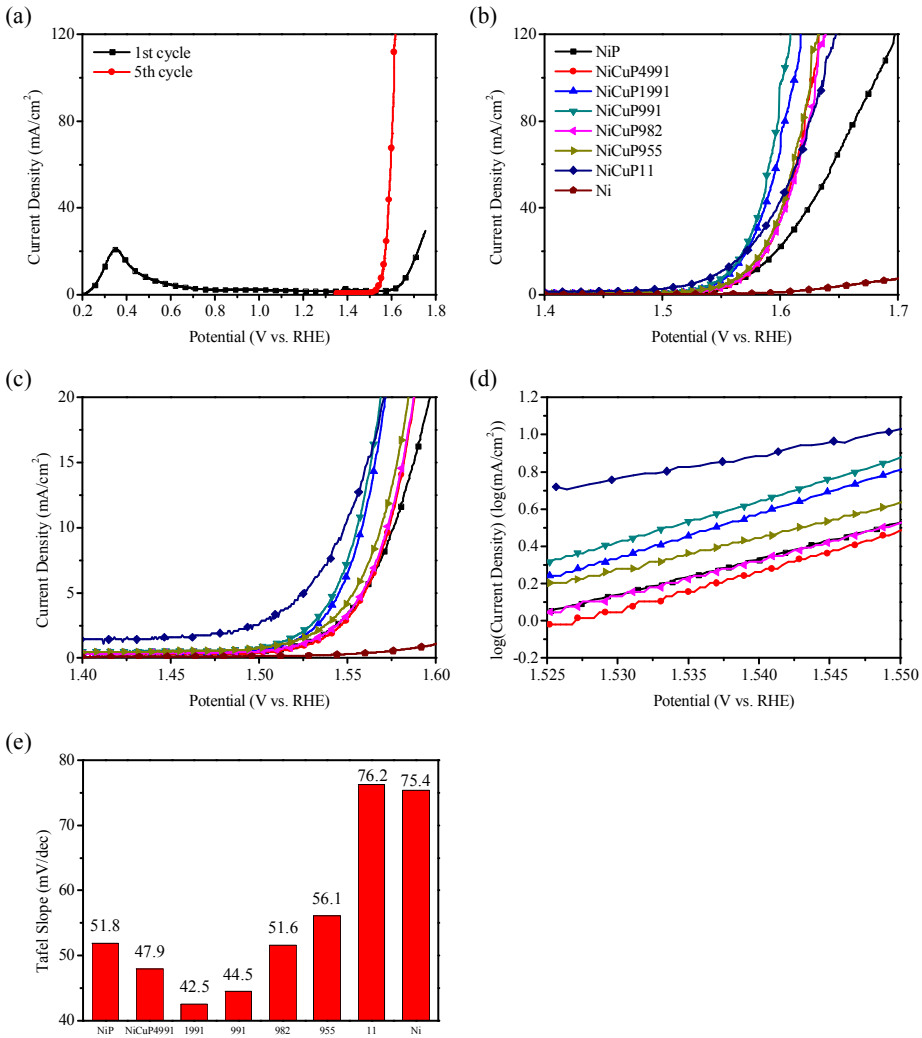

Fig. 3.3 (a) 1st cycle and 5th cycle of polarization curve for NiCuP1991, (b) polarization curves, (c) inlet of (b), (d) Tafel plots and (e) Tafel slopes of deposits prepared by various Ni/Cu ratios.

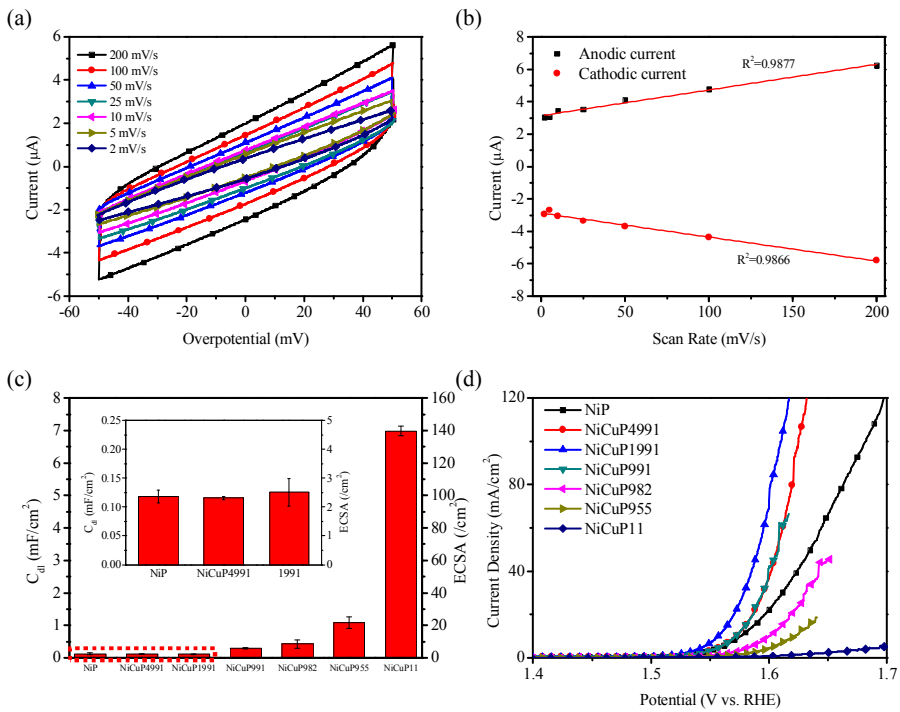

Fig. 3.4 (a) Typical cyclic voltammetry of NiCuP1991 in potential range between 0.05 V ~ -0.05 V (vs. OCP), (b) I_0 vs ν plot for (a), (c) C_{dl} and ECSA of catalysts of various Ni/Cu ratios (inlet: expanded for NiP, NiCuP4991 and

NiCuP1991) and (d) “normalized” polarization curve assuming all of catalysts embrace same surface area with NiP.

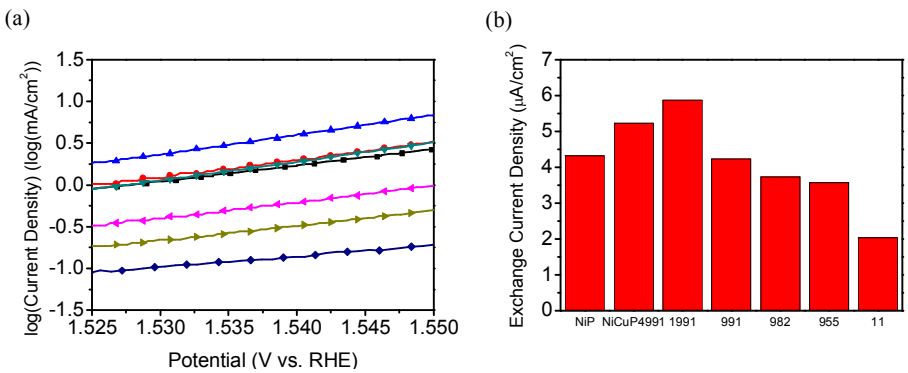

Fig. 3.5 (a) Tafel plot obtained from "normalized" polarization curve (Fig. 3.4 (d)) and (b) exchange current density (i_0) calculated from intercept of Tafel plot.

3.3 Characterization of Catalyst

Surface images were shown in Fig 3.5 taken with scanning electron microscope for as-prepared NiP, NiCuP4991, NiCuP1991, NiCuP991 and NiCuP955. Apparent morphology of NiP, NiCuP4991 and NiCuP1991 did not show remarkable difference, while clearly expanded surface area were observed for NiCuP991 and NiCuP955. These results are definitely supporting the surface area trend displayed in Fig. 3.4 (c). Cross-sectional SEM images of NiP and NiCuP1991 revealed that deposited catalysts exist in the type of film. Thicknesses of NiP and NiCuP1991 were measured as 458.6 (± 16.48) nm and 478.3 (± 37.21) nm, respectively.

Energy dispersive X-ray spectroscopy mapping indicates that main elements (Ni, Cu, P and O) are distributed uniformly throughout the surface. (Fig. 3.6) Even though Cu was not contained in NiP preparing solution, Cu was detected in mapping results. This is not due to imperfect coverage of catalyst, but because of relative thin catalyst layer (< 500 nm) and large penetration depth (> 4 μm at 15 kV acceleration voltage) of electron beam in the detecting condition. Hence, it was

turned to be challenging, unfortunately, to confirm quantitative ratio between Ni and Cu precisely.

SEM and EDS analysis were also conducted for catalysts after 2 hr OER operation at 10 mA/cm^2 current density. Fig. 3.7 shows surface SEM images after OER for NiP and NiCuP1991. For both catalysts, surface morphology remained same upon the operation. All of main elements are still distributed impartially over the surface. Widely known fact is that OER catalysts suffer surface deformation upon the operation. Oxygen content in surface generally increases significantly as the operation was performed. Phosphorous in alloy naturally undergoes dissolution upon oxidation, which is verified by the replacement of outmost surface layer by NiOOH. According to several previous reports, phosphorous containing layer lies very underneath the NiOOH layer, supporting high OER catalytic activity.[20] Hence, severe dissolution of phosphorous may cause decrease in catalytic activity. EDS atomic ratio of phosphorous and oxygen were suggested in Table 3.1. Both NiP and NiCuP1991 showed increased oxygen contents, as a result of oxidation. Although oxygen content in as-prepared NiCuP1991 was lower than that of NiP, post-OER oxygen content of NiCuP1991 was much higher than that of NiP. Unlike oxygen, phosphorous content showed only slight decrease after 2 hr operation.

For the sake of analyzing detailed surface composition, X-ray photoelectron spectroscopy analysis was conducted. Fig. 3.8 shows survey XPS spectra of as-prepared NiP and NiCuP1991. High-resolution XPS spectra were shown in Fig. 3.9. Ni $2p_{3/2}$ spectrum is divided into Ni, NiO_x(NiO and $Ni(OH)_2$), Ni^{3+}(NiOOH) and satellite peak of Ni. Ni peak at 852.8 eV is slightly shifted toward positive side compared to Ni metallic peak (852.4 eV). Analyzing oxidation state of Ni was complicated due to formation of native oxide (853.6 eV) and Ni-P (856.8 eV) phase. Two different oxidation states were observed for phosphorous, which are revealed as phosphate (133.0 eV) and phosphorous (129.7 for $2p_{3/2}$ and 130.6 eV for $2p_{1/2}$). Putting these results together, Ni-P phase was successfully deposited on the substrate. It is also worth noting that Cu was not detected at all in NiP spectra, despite Cu foil was used as a substrate. This implies that perfect coverage was achieved for catalyst deposition. Spectra of NiCuP1991 generally showed similar aspects to that of NiP. In contrast to NiP, Cu peak was observed for NiCuP1991, which is shown in Fig. 3. 9 (b). When OER was performed for these catalysts, surface oxidation occurs during the operation. Changes in surface affects stability upon long-term operation as well as catalytic activity. Fig. 3.10 indicates XPS survey spectra for NiP and NiCuP1991 after 10 mA/cm^2 OER operation for 2 hrs. High resolution spectra shown in Fig. 3.11 clearly reveals oxidation of the surface.

Ni metallic peak disappeared for both NiP and NiCuP1991, while NiO_x became predominant state. Ni^{3+} (NiOOH) peak emerged after OER, which is related to early-reported surface oxidation of Ni species during OER. Stronger Ni^{3+} (NiOOH) peak was detected in NiCuP1991 case, which corresponds to higher oxygen content in elemental mapping data. Since outermost NiOOH layer is directly responsible for oxygen evolution, increase in proportion of NiOOH enabled higher catalytic activity.[16,19-20], Phosphorous peaks were not observed for NiP catalyst, while phosphate still remains on the surface. In NiCuP1991, phosphate peak was detected only in negligible level, nor was phosphorous. This is related to NiOOH layer formation upon oxidation of surface concurrent with phosphorus dissolution, which is also consistent with previous reports.[16,17,20]

Crystalline structures of catalysts were investigated with X-ray diffraction. Fig. 3. 12 compares diffraction patterns of NiP and NiCuP1991 with Cu and Ni foil. It is remarkable that even though Ni was successfully deposited on Cu foil, no peak related to Ni was observed for both NiP and NiCuP1991. It implies that Ni species were deposited as nano-crystalline phase unlike other early reported materials. Peak intensity of Cu (200) was decreased significantly upon deposition, (see Table 3.2.) which is referred to blockage of surface by catalyst deposit. XRD patterns of catalysts went through 2 hr of OER were indicated in Fig. 3.13. No obvious

difference was found with peak location, while intensity of Cu(200) increased significantly after OER. Peak intensity of Cu(200) even surpassed that of Cu foil substrate, which suggests recrystallization upon the OER.

Impedance spectroscopy was used to estimate charge transfer resistance of catalysts. Nyquist plots of NiP and NiCuP1991 in alkaline solution are shown in Fig. 3.14. Simulation results demonstrate that semicircle diameter of NiCuP1991 is smaller than that of NiP, which are calculated as 121.7 (±7.378) and 201.9 (±15.87) Ω/cm^2, respectively.

Table 3.1 Elemental Atomic Percent of Phosphorous and Oxygen for As-prepared and After 2 hr OER.

	P		O	
	As-prepared	2 hr OER	As-prepared	2 hr OER
NiP	8.14	7.80	12.95	19.89
NiCuP1991	8.13	7.53	8.03	34.53

Table 3.2 XRD Peak Intensities of Cu(111), Cu(200) and Cu(220) for NiP, NiCuP1991 and Cu Foil.

Intensity	Cu(111)	Cu(200)	Cu(220)
Cu foil	234	556854	227
NiP_As	163	71216	154
NiP_2 hr	108	177260	307
1991_As	89	15496	107
1991_2 hr	306	99837	128

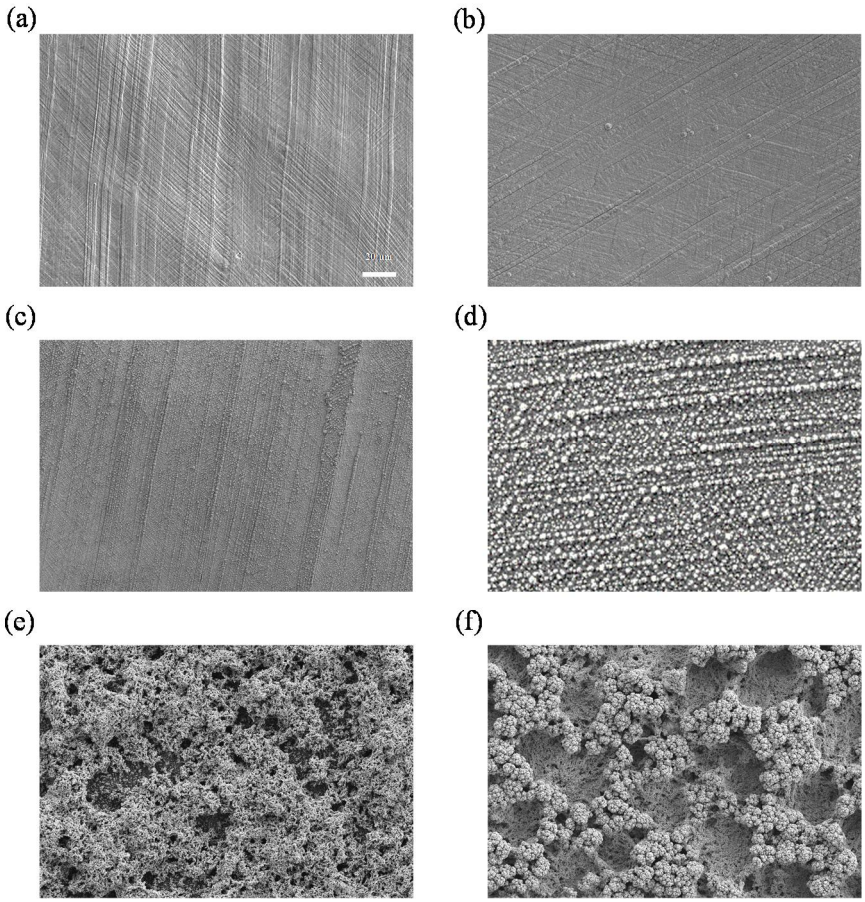

Fig. 3.6 Surface SEM images of (a) NiP, (b) NiCuP4991, (c) NiCuP1991, (d) NiCuP991, (e) NiCuP955 and (f) NiCuP11.

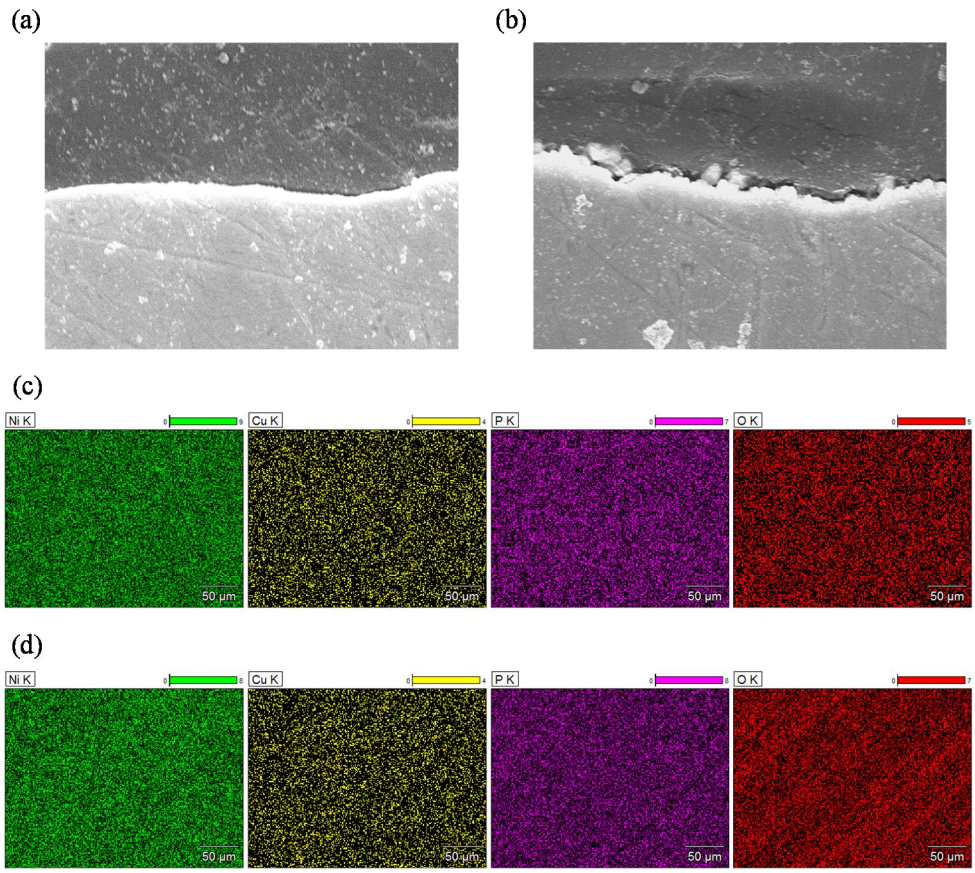

Fig. 3.7 Cross-sectional SEM images of as-prepared (a) NiP, (b) NiCuP1991, EDS mapping results of (c) NiP and (d) NiCuP1991.

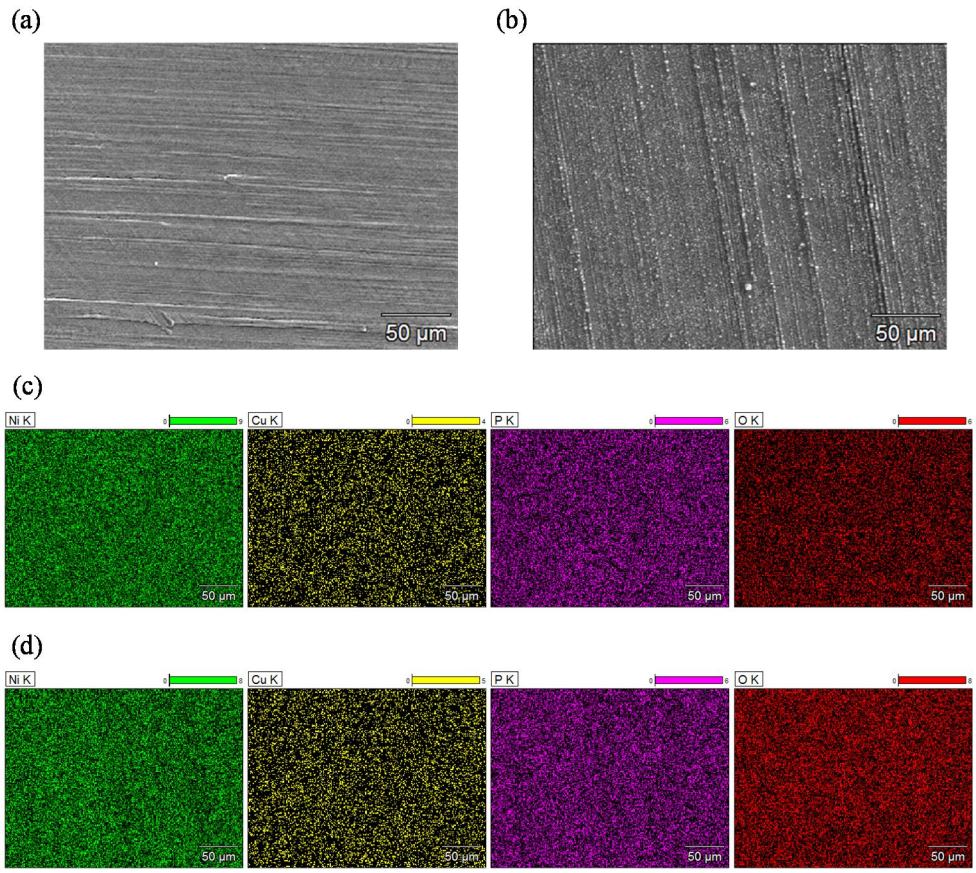

Fig. 3.8 Surface images of post-2 hr OER (a) NiP, (b) NiCuP1991, EDS mapping results of (c) NiP and (d) NiCuP1991.

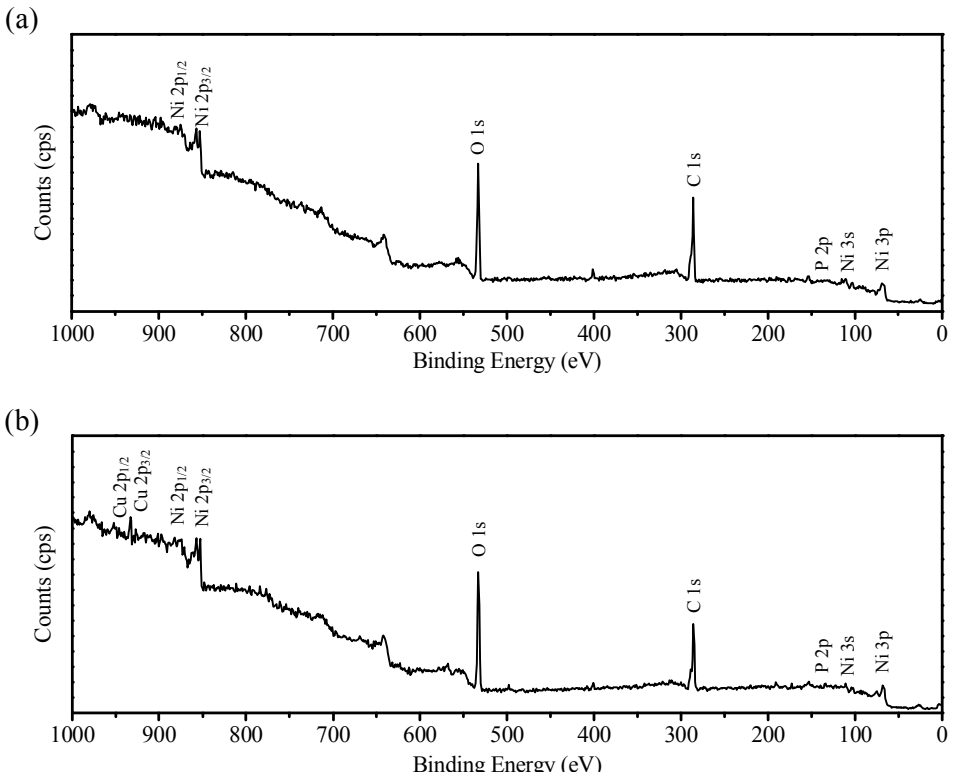

Fig. 3.9 XPS survey spectra for as-prepared (a) NiP and (b) NiCuP1991.

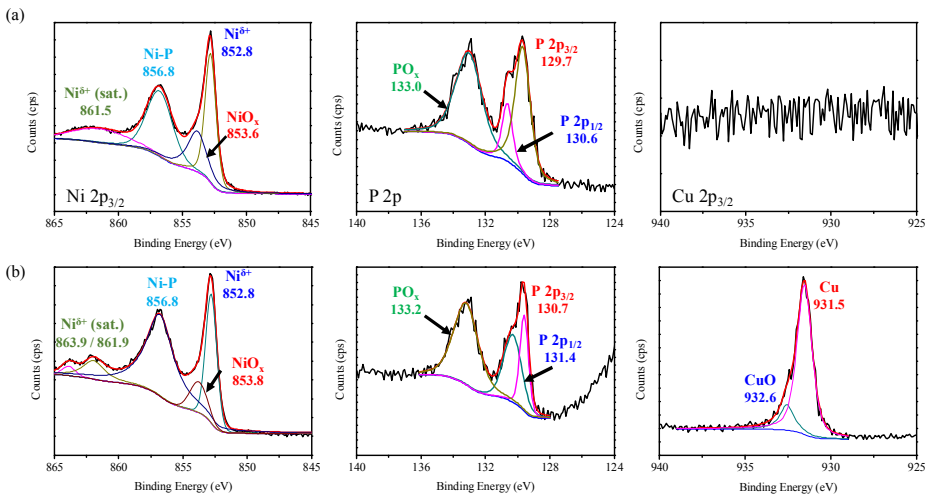

Fig. 3.10 High-resolution XPS spectra shown for Ni $2p_{3/2}$, P 2p and Cu $2p_{3/2}$ regions (left to right) for as-prepared (a) NiP and (b) NiCuP1991.

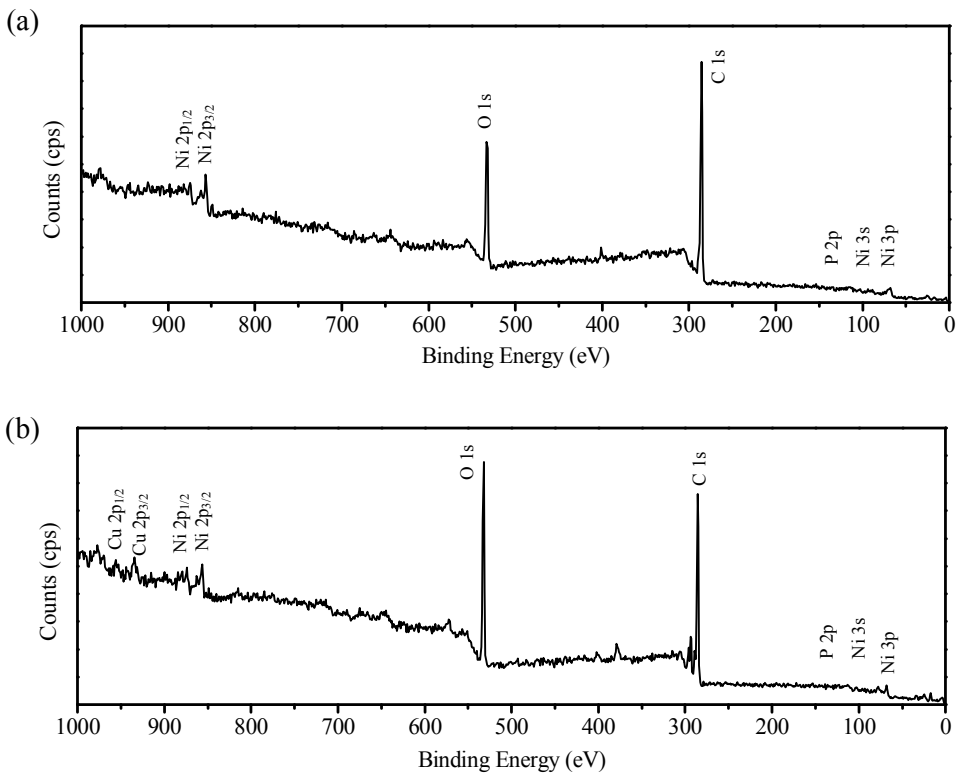

Fig. 3.11 XPS survey spectra for post-2 hr OER (a) NiP and (b) NiCuP1991.

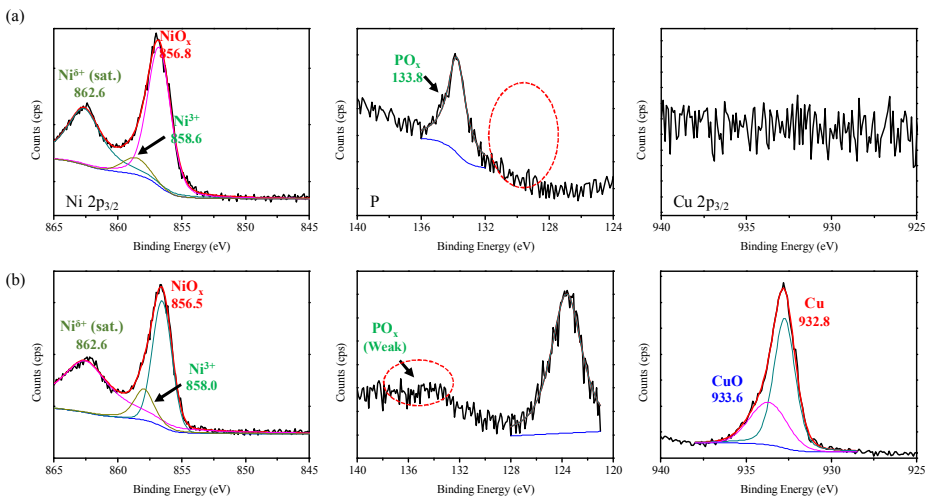

Fig. 3.12 High-resolution XPS spectra shown for Ni $2p_{3/2}$, P 2p and Cu $2p_{3/2}$ regions (left to right) for post-2 hr OER (a) NiP and (b) NiCuP1991.

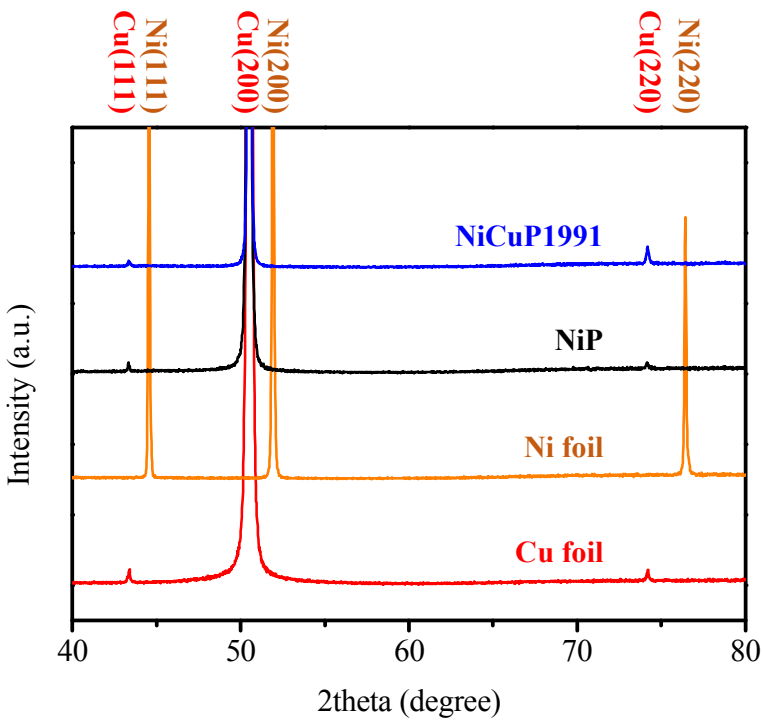
Ni(111)
Cu(111)
Ni(200)
Cu(200)
Ni(220)
Cu(220)
NiCuP1991
NiP
Ni foil
Cu foil
Intensity (a.u.)
40
50
60
70
80
2theta (degree)

Fig. 3.13 XRD patterns of as-prepared NiP and NiCuP1991. Patterns of Ni foil and Cu foil were given for reference.

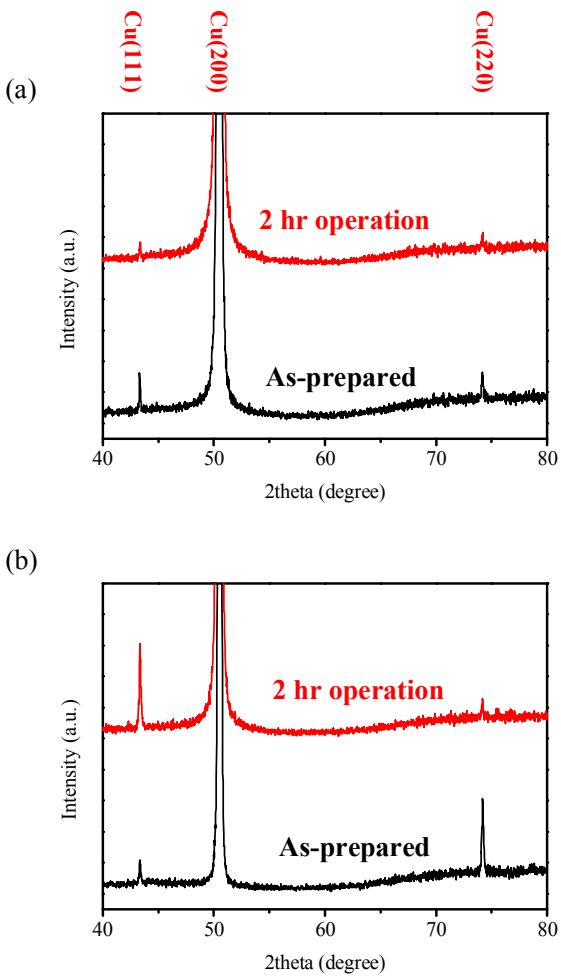

Fig. 3.14 XRD patterns of as-prepared and post-2 hr OER catalysts for (a) NiP and (b) NiCuP1991.

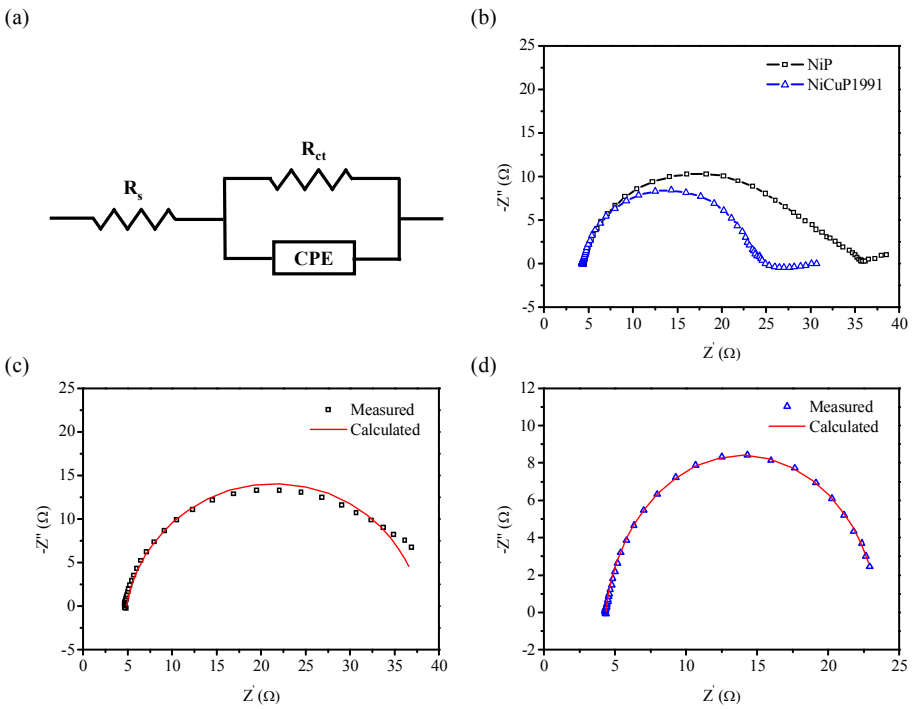

Fig. 3.15 Impedance studies of NiP and NiCuP1991. (a) equivalent circuit applied, (b) Nyquist plot of NiP and NiCuP1991 (100 kHz ~ 0.1 Hz), comparison with fitting results of Nyquist plot (100 kHz ~ 100 Hz) of (c) NiP and (d) NiCuP1991.

3.4. Faradaic Efficiency Calculation

To estimate Faradaic efficiency of the catalyst, gas chromatography (GC) was used for measurement of evolved oxygen. Fig. 3.15 illustrates chromatogram of GC analysis, which indicates evolution of oxygen peak in every 3 min. Since current was set as constant of 10 mA, oxygen generation assuming 100% Faradaic efficiency may be calculated. Practically measured oxygen is estimated with conversion of oxygen peak area to volumetric fraction of oxygen, using 20.95% of oxygen ratio of fresh air as a reference. As shown in Fig. 3.15, oxygen peak emerges as the time increases, then becomes saturated after 6 min of operation. Oxygen peak intensity attains maximum as the system reaches steady-state, which means that generation rate on the electrode becomes equivalent to output rate. Smaller oxygen peak at earlier stage (< 6 min) is because surface was being oxidized prior to OER or steady-state had still not achieved in short time period. Fig. 3.16 compares calculated and measured amount of oxygen. Measured oxygen literally approaches the calculated amount, as shown in the figure. Faradaic

efficiency was calculated with dividing measured oxygen by calculated one, which also reaches nearly 100% (99.13% at 51 min). Although Faradaic efficiency was lower in early stage due to surface oxidation, it is apparent to all that efficiency reaches 100% after the system becomes stable.

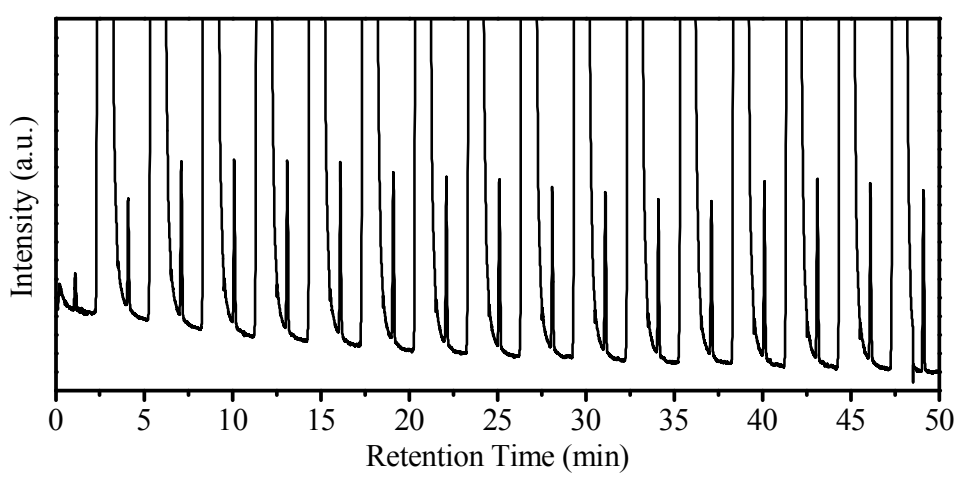

Fig. 3.16 Gas chromatogram of oxygen evolution experiment up to 51 min.

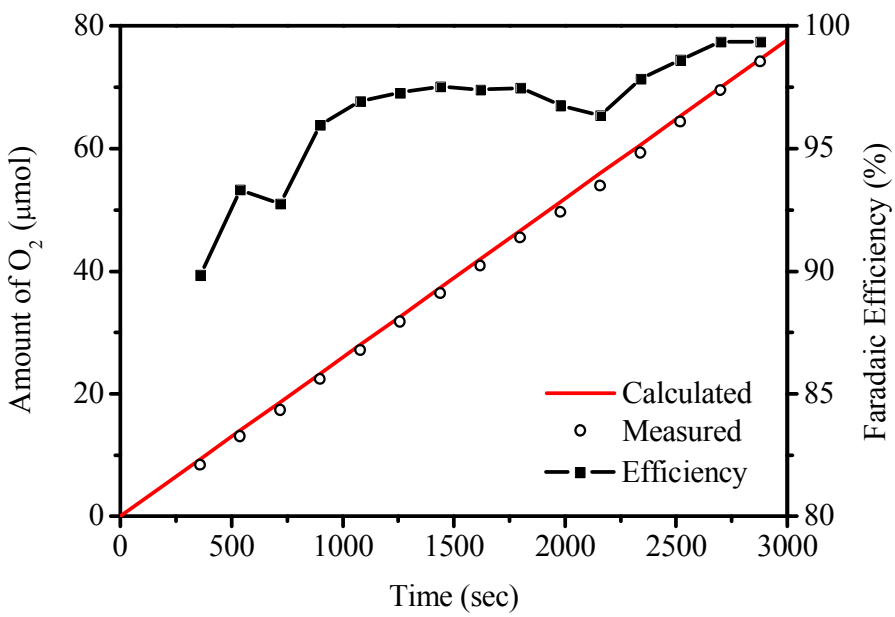

Fig. 3.17 Amount of evolved oxygen gas as a function of operation time.

Chapter 4. Conclusion

The nickel-copper phosphorous electrocatalyst was successfully synthesized with facile electrodeposition. Optimization of deposition condition found that catalyst prepared by electrolyte containing 199:1 ratio of Ni and Cu source (NiCuP1991) exhibited the best performance toward OER. NiCuP1991 had uniform film-like morphology with approximately 478.3 nm thickness, according to SEM-EDS analysis. Electrochemical analyzes such as linear sweep voltammetry and impedance study confirmed higher catalytic activity of NiCuP1991 over NiP, which is earlier reported as efficient OER electrocatalyst. Tafel slope of NiCuP1991 (42.5 mV/dec) was lower than that of other catalysts with different Ni/Cu ratio (44.5 ~76.2 mV/dec) as well as NiP (51.8 mV/dec). Although NiCuP991 (99:1 of Ni/Cu source ratio) delivered higher apparent current than that of NiCuP1991, NiCuP1991 exhibited the most superior current density when

assuming the same surface area. XPS analysis confirmed that as copper was introduced to the catalyst, high valence state (Ni^{3+}) of Ni species are stabilized and thus distributed more on the surface compared to NiP, which results in higher catalytic activity with lower Tafel slope and charge transfer resistance. Additional spectroscopic analyzes including XRD were performed in order to characterize the as-prepared and post-OER catalysts. XRD patterns showed that NiCuP1991 exists as nano-crystalline phase, since there was no noticeable Ni related peak. Nickel-copper phosphorous maintained its catalytic activity as well as surface morphology after long term operation at 10 mA/cm^2 current density up to 18 hours. While NiP required 13 mV of additional overpotential after 18 hours of OER, only 7 mV of overpotential increase was observed for NiCuP1991. Faradaic efficiency of NiCuP1991 catalyst was estimated as nearly 100% (99.13% after 51 min), which is confirmed by gas chromatography experiment.

Bibliography

1. International Energy Agency, World Energy Outlook Special Report 2016: Energy and Air Pollution (2016).

2. B. E. Conway and T. C. Liu, *Langmuir*, **6**, 268 (1990).

3. V. I. Birss, A. Damajanovic and P. G. Hudson, *J. Electrochem. Soc*., **133**, 1621 (1986).

4. M. Gao, W. Sheng, Z. Zhuang, Q. Fang, S. Gu, J. Jiang and Y. Yan, *J. Am. Chem. Soc*., **136**, 7077 (2014).

5. T. Reier, M. Oezaslan and P. Strasser, *ACS Catal*., **2**, 1765 (2012).

6. A. Damjanovic, L. –S. R. Yeh and J. F. Wolf, *J. Electrochem. Soc*., **127**, 1945 (1980).

7. V. I. Birss and A. Damajanovic, *J. Electrochem. Soc*., **134**, 113 (1987).

8. M. E. G. Lyons and S. Floquet, *Phys. Chem. Chem. Phys*., **13**, 5314 (2011).

9. S. Gottesfeld and S. Srinivasan, *J. Electroanal. Chem*., **86**, 89 (1978).

10. D. A. Corrigan and R. M. J. Bendert, *J. Electrochem. Soc*., **136**, 723 (1989).

11. M. D. Merrill and R. C. Dougherty, *J. Phys. Chem. C*, **112**, 3655 (2008).

12. J. C. Ho and D. L. Piron, *J. Appl. Electrochem*., **26**, 515 (1996).

13. X. Lu and C. Zhao, *Nat. Commun*., **6**, 6616 (2015).

14. M. Gong, Y. Li, H. Wang, Y. Liang, J. Z. Wu, J. Zhou, J. Wang, T. Regier, F. Wei and H. Dai, *J. Am. Chem. Soc*., **135**, 8452 (2013).

15. K. Fan, H. Chen, Y. Ji, H. Huang, P. M. Claesson, Q. Daniel, B. Philippe, H. Rensmo, F. Li, Y. Luo and L. Sun, *Nat. Commun*., **7**, 11981 (2016).

16. B. You, N. Jiang, M. Sheng, M. W. Bhushan and Y. Sun, *ACS Catal*., **6**, 714 (2016).

17. N. Jiang, B. You, M. Sheng and Y. Sun, *Angew. Chem. Int. Ed*., **54**, 6251 (2015).

18. Q. Liu, S. Gu and C. M. Li, *J. Power Sources*, **299**, 342 (2015).

19. X. Wang, W. Li, D. Xiong and L. Liu, *J. Mater. Chem. A*, **4**, 5639 (2016).

20. L. Stern, L. Feng, F. Song and X. Hu, *Energy Environ. Sci*., **8**, 2347 (2015).

21. E. J. Popczun, J. R. McKone, C. G. Read, A. J. Biacchi, A. M. Wiltrout, N. S. Lewis and R. E. Schaak, *J. Am. Chem. Soc*., **135**, 9267 (2013).

22. Z. Xing, Q. Liu, A. M. Asiri and X. Sun, *Adv. Mater*., **26**, 5702 (2014).

23. M. T. Tavares and C. A. Bernardo, *J. Catal*., **100**, 545 (1986).

24. S. Hufner, G. K. Wertheim and J. H. Wernick, *Phys. Rev. B*, **8**, 4511 (1973).

25. A. R. Nagahash, T. H. Etsell and S. Xu, *Chem. Mater*., **18**, 2480 (2006).

26. A. Van der Ven, D. Morgan, Y. S. Meng and G. Ceder, *J. Electrochem. Soc*., **153**, A210 (2006).

27. L. M. Abrantes and J. P. Correia, *J. Electrochem. Soc*., **141**, 2356 (1994).

28. European Space Agency, Supporting Education Across Europe Impress, (http://www.spaceflight.esa.int/impress/text/education/Solidification/Phase_Diagrams.html)

29. University of Rhode Island, Chemistry 112 Reference Materials (http://bilbo.chm.uri.edu/CHM112/index.html)

30. X. Wang, W. Li, D. Xiong, D. Y. Petrovykh and L. Liu, *Adv. Funct. Mater.*, **26**, 4067 (2016).

31. C. C. L. McCrory, S. Jung, J. C. Peters and T. F. Jaramillo, *J. Am. Chem. Soc*., **135**, 16977 (2013).

초 록

전기화학적 물 분해는 수소의 대량 생산에 적용할 수 있는 가장 유력한 후보로 꼽히고 있다. 하지만 물의 전기분해는 산소 발생 반응(OER)의 느린 전자 전달로 인한 에너지 효율이 감소하고, 효율적으로 알려진 촉매들이 고가라는 점에서 단점을 내포하고 있다. 때문에 많은 연구자들이 저렴한 가격으로 형성한 고활성 전기화학 촉매 개발에 힘쓰고 있다. 이에 본 연구에서는 간편한 전기도금 방법으로 높은 OER 활성을 가지는 니켈-구리 인화촉매를 제조하는 것을 목표로 하였다. 실험 조건의 최적화 결과 니켈과 구리를 199:1 의 비율로 포함한 용액에서 전해 도금을 진행한 촉매가 가장 좋은 활성을 보였으며, 이미 좋은 OER 촉매로 알려진 NiP 보다 우수한 활성을 나타내었다. 적절한 양의 구리를 첨가하면 Tafel 기울기와 함께 전자 전달 저항이 감소하는 것을 확인하였다. XPS 분석을 통해 구리를 첨가할 경우 더 많은 양의 고산화된 니켈이 표면에서 검출되어, OER 반응 중 Ni 의 최외곽에 형성되는 열역학적으로 불안정한 높은 산화 상태의 니켈 수산화물을

효율적으로 지지해주는 것으로 보인다. XRD 분석을 통해 제조한 촉매는 무수히 작은 나노 크기의 결정을 가지고 있는 것으로 생각되었다. SEM 을 통해 제조된 촉매가 얇은 막 형태로 도금 된 것을 확인하였고, 포함된 모든 원소들은 표면에 고르게 분포하였다. 제조한 촉매는 18 시간의 OER 반응 하에서도 안정성을 잘 유지하였고, 99% 이상의 높은 전하 효율을 보여주었다.

주요어: 니켈-구리 인화물, 산소 발생 반응 (OER), 전기도금, 전기화학적 물 분해, 전기화학 촉매

학 번: 2015-21045